SLAC-R-556
UC-414

Precise Measurement of the Left-Right Asymmetry in Z^0 Boson Production by e^+e^- Collisions. Electron Beam Polarization Measurement with the Quartz Fiber Calorimeter.*

D. V. Onoprienko

Stanford Linear Accelerator Center
Stanford University
Stanford, CA 94309

SLAC-Report-556
August 2000

Prepared for the Department of Energy
under contract number DE-AC03-76SF00515, DE-AC05-96OR22464,
DE-FG05-91ER40627.

Printed in the United States of America. Available from the National Technical Information Service, U.S. Department of Commerce, 5285 Port Royal Road, Springfield, VA 22161.

---

[*] Ph.D. thesis, Stanford Linear Accelerator Center, Stanford, CA 94309.

Acknowledgments

I would like to thank my advisor, William Bugg, for making it possible for me to spend nearly four years at SLAC working on this project, and for his guidance and support during this time. His enthusiasm and taste for good physics were truly inspiring; his ideas and suggestions were always timely and fruitful.

While it is clearly impossible to mention all people who contributed to the success of the experiment, there are a few whom I'd like to give my special thanks.

Peter Rowson led the SLD Electroweak group. If not for his extraordinary enthusiasm and determination to finally get the things done, the analysis would probably never be finalized, and we would still be discussing some of the instrumental problems that blocked the way to physics.

Mike Woods taught me a lot about polarimetry and the SLC; his advice was always extremely helpful, and his attention to details improved greatly the quality of the analysis we worked on.

Yuri Kamyshkov and Yuri Efremenko thought up and built the QFC polarimeter; together with Bill Bugg, Steve Berridge, Hans Cohn, Kostya Shmakov, and Achim Weidemann, they helped to make it work.

Various pieces of the polarimetry and the A^0_{LR} analyses were contributed by Rob Elia, Jorge Fernandez, Mike Fero, Ray Frey, Tom Junk , Ross King, Amitath Lath, Per Reinertsen, Bruce Schumm, Morris Swartz, Eric Torrence, and other members of the SLD Electroweak group.

Contents

List of Tables

List of Figures

Chapter 1

Introduction

The completion of the SLD experiment marks the end of a very productive decade of the Z-pole physics, which brought dramatic improvements in the accuracy of electroweak measurements. Experimental study of the $e^+e^- \longrightarrow Z^0 \longrightarrow f\bar{f}$ process, started about 11 years ago by the Mark II collaboration, proved to be an excellent source of electroweak information. The SLD and the four LEP experiments are now wrapping up their Z-pole data analyses. This thesis presents the final results of the left-right Z^0 boson production cross section asymmetry (A^0_{LR}) measurement (which is unambiguously related to the effective electroweak mixing angle, $\sin^2\theta_W^{eff}$), based on the full data sample collected by the SLD collaboration.

I will focus on the two latest SLD runs: 1996 and 1997/98. The analysis procedures used in previous runs are described in the theses by Ross King [1], Amitabh Lath [2], Robert Elia [3], and in the three Physical Review Letters [4, 5, 6].

The last two runs increased the SLD data sample by more than a factor of 3, and involved many changes in both the hardware used in the experiment, and in the analysis techniques. They were also used to carry out a number of studies addressing various potential sources of systematic errors of the A_{LR}^0 measurement - positron beam polarization, energy spectrometers calibration, and polarimetry related uncertainties.

One of the critical - and most difficult - pieces of the A_{LR}^0 analysis is the electron beam polarization measurement performed by the Compton polarimeter. Even though the polarimeter hardware (the laser system and the Čerenkov electron detector, called CKV) did not undergo major changes in recent years, changes in the accelerator setup had substantial effect on the polarimeter operation, forcing the group to cope with new mysteries that popped up in each SLD run. The term "channel-to-channel consistency" (or "inconsistency", depending on how we were doing at the time) was probably one of the most frequently heard expression during the Compton meetings. In 1997/98, when efforts by the SLC machine physicists finally paid off, and the luminosity exceeded the 200 Z/hour threshold (compared to about 50 Z/hour maximum observed in previous years), the polarimeter background levels jumped up by orders of magnitude as a result of larger focusing angles at the SLD IP. An attempt to solve the problem by installing a larger diameter beam pipe in the polarimeter region was aborted due to engineering difficulties, and the accelerator had to be run in the "electrons only" mode for 3 minutes every hour to ensure reliability of the polarization monitoring.

Given the critical role played by the polarization measurement in the SLD physics program, it was highly desirable to perform an independent cross check of the measurement provided by the Compton polarimeter. With the polarimeter analyzing power calibration problems we experienced during the last two runs, it became clear that achieving the target 0.5 % precision (that would guarantee that the A^0_{LR} measurement accuracy was not limited by systematics) was hardly possible based on the CKV detector results alone. To perform a cross check, we designed, built, and operated the Quartz Fiber Calorimeter (QFC) polarimeter, which is discussed in detail in chapter 4. The QFC detects Compton scattered photons and determines the longitudinal polarization of the electron beam by measuring the asymmetry in the energy flow between the two possible electron-photon helicity combinations. The calorimeter is designed to be position sensitive in both vertical and horizontal directions in order to also detect the angular asymmetry and thus measure the transverse polarization, which would be very useful for better understanding spin transport through the collider arcs, and for tuning the spin orientation at the SLD IP.

The idea of using a total absorption calorimeter in a Compton polarimeter was first described by C. Prescott [7] in 1973, and a conceptual design of a photon detector for the SLD polarimeter was proposed in 1993 by M. Fero et al. [8]. At that time, however, feasibility study showed that implementing such detector for use in the SLC Final Focus environment was highly problematic, primarily due to background and radiation damage related issues. In 1994, the University of Tennessee group originated the QFC design proposal, which attempted to resolve these problems. The detector was built and installed in the SLC in 1995, and commissioned during the SLD 1996 run. Based on the results of the commissioning, the detector was modified, and additional shielding was installed in the area. We took the data used for comparison with the CKV detector in 1997, and then brought the calorimeter to the FFTB facility at SLAC for a beam test in order to study its response function and other sources of systematic errors. Based on the data taken with the QFC during the 1997/98 run, we were able to cross check the polarization measurement by the CKV detector with sub-1 % precision. The QFC thus became the first successful implementation of a high precision calorimeter-based Compton polarimeter. Combined with other improvements in the polarimetry analysis, the QFC results allowed us to achieve the target 0.5 % overall polarization measurement accuracy.

The QFC detector sensitivity to the transverse component of the polarization has been demonstrated, even though a precise measurement could not be performed, primarily because of operational difficulties caused by the necessity to avoid interference with other detectors located in the polarimeter area.

Thesis outline

Chapter 2 describes physics motivation for the A_{LR} measurement, and the process of extracting the A^0_{LR} from the observed asymmetry in Z^0 production. I tried to make this chapter very brief, and to avoid describing the Standard Model itself whenever possible, since the model has been essentially unchanged for many years, and a number of excellent books have been written on this subject (see, for example, [9] and [10]).

Chapter 3 is devoted to the four major hardware components involved in the A_{LR}^0 measurement: the SLAC Linear Collider, the WISRD energy spectrometers, the SLD detector, and the Compton polarimeter. The emphasis is on recent changes, studies and developments.

Chapter 4 provides a technical description of the polarization measurement with the QFC detector: calorimeter design, operation, and analysis procedures. Results of comparison with the SLD's standard CKV polarimeter are presented.

Chapter 5 describes the technique used for measuring the experimental asymmetry in Z^0 boson production: triggers, event selection, and background estimation.

Chapter 6 describes the procedure for extracting the A_{LR}^0 from the observed asymmetry in Z^0 production: correcting for instrumental asymmetries, and calculating the Z-pole value of A_{LR} The final results are presented for the measured A_{LR}^0 and the weak mixing angle.

Finally, chapter 7 discusses the results and compares them to measurements by other experiments, as well as to the Standard Electroweak Model predictions.

Chapter 2

Physics motivation

The principal goal of the SLD electroweak physics program is to test the validity of the Standard Model (introduced by Glashow [11], Weinberg [12], and Salam [13]), and to search for new physics phenomena beyond the Standard Model.

There are two possible approaches to the task. The direct one is to search for new particles and effects, and this method proved to be fruitful in the past - the discovery of W and Z bosons was a triumph of the Glashow-Weinberg-Salam theory, and a boost for new theoretical developments. There is still a critical component of the Standard Model that has not been observed experimentally - the Higgs boson. However, the A_{LR}^0 measurement efforts take another approach - precise determination of the Standard Model parameters, which allows to test the model for self-consistency, and search for new physics that might manifest itself in deviations from the behavior predicted by the Model. The measurement of A_{LR}^0 (which is by definition unambiguously related to the effective weak mixing angle $sin^2\theta_W^{eff}$) is a particularly sensitive probe, as will be explained below. However, it should be noted that since the Standard Model prediction for the exact value of $sin^2\theta_W^{eff}$ depends on the unknown mass of the Higgs boson, a single A_{LR}^0 measurement alone does not test the model - it is only meaningful when compared to measurements based on other phenomena, and to the measured values of other electroweak parameters.

In this chapter, we will briefly describe the Standard Model, discuss the physics that can be explored by the experimental study of the $e^+e^- \longrightarrow Z^0 \longrightarrow f\bar{f}$ process, and describe various aspects of extracting A_{LR}^0 from the left-right asymmetry in Z^0 boson production measured by the SLD experiment. The consistency of the measured $sin^2\theta_W^{eff}$ value with the Standard Model predictions will be discussed in chapter 7.

2.1 Standard Model of electroweak interactions

The Standard Model is a non-Abelian gauge theory based on the SU(2)×U(1) group. W_μ^i $(i = 1, 2, 3)$ and B_μ are the gauge bosons of the SU(2) and U(1) groups, respectively. The corresponding gauge coupling constants are g and g'. The symmetry is broken spontaneously by introducing a scalar field ϕ that transforms as a spinor under SU(2) and acquires a vacuum expectation value of the form

$$< \phi >= \frac{1}{\sqrt{2}} \begin{pmatrix} 0 \\ v \end{pmatrix} \tag{2.1}$$

The symmetry breaking results in two charged massive vector bosons

$$W_\mu^\pm \equiv \frac{1}{\sqrt{2}}(W_\mu^1 \mp iW_\mu^2) \tag{2.2}$$

with masses

$$M_W = g\frac{v}{2} \tag{2.3}$$

and two neutral vector boson fields

$$\begin{aligned} Z_\mu^0 &\equiv -B_\mu \sin\theta_W + W_\mu^3 \cos\theta_W \\ A_\mu &\equiv B_\mu \cos\theta_W + W_\mu^3 \sin\theta_W \end{aligned} \tag{2.4}$$

with masses

$$\begin{aligned} M_Z &= \frac{v}{2}\sqrt{g^2 + g'^2} \\ M_A &= 0 \end{aligned} \tag{2.5}$$

where θ_W is the weak mixing angle defined as $\theta_W \equiv \arctan(g'/g)$. The massless A_μ field is identified as the electromagnetic vector potential, and the positron electron charge is given by $e = g\sin\theta_W$. The only part of ϕ that remains after spontaneous symmetry breaking is the neutral Higgs boson H whose mass is not predicted by the theory.

The left-handed fermions appear as SU(2) doublets $\psi_i = \begin{pmatrix} \nu_i \\ \ell_i^- \end{pmatrix}$ and $\psi_i = \begin{pmatrix} u_i \\ d_i \end{pmatrix}$, while the right-handed fields are SU(2) singlets. In the minimal model, there are 3 generations of fermions.

The Lagrangian is given by

$$\begin{aligned}\mathcal{L} = \; & \sum_f \bar{\psi}_f \left(i \not{\partial} - m_f - \tfrac{g m_f H}{2 M_W} \right) \psi_f - \\ & - \frac{g}{2\sqrt{2}} \sum_f \bar{\psi}_f \gamma^\mu (1 - \gamma^5)(T^+ W^+_\mu + T^- W^-_\mu) \psi_f - \\ & - e \sum_f q_f \bar{\psi}_f \gamma^\mu \psi_f A_\mu - \\ & - \frac{g}{2\cos\theta_W} \sum_f \bar{\psi}_f \gamma^\mu (v_f - a_f \gamma^5) \psi_f Z_\mu \end{aligned} \tag{2.6}$$

where $T^{\pm}$ are the weak isospin raising and lowering operators; q_f, v_f, and a_f are the charge (in units of e) and the vector and axial couplings of the particular fermion in question. v_f and a_f are given by

$$\begin{aligned} v_f &\equiv t^3_f - 2 q_f \sin^2\theta_W \\ a_f &\equiv t^3_f \end{aligned} \tag{2.7}$$

where t^3_f is the weak isospin of the fermion.

Not counting the Higgs boson mass and fermion masses and couplings, the Standard Model has three parameters. A widely used set of parameters includes the fine structure constant α, the Fermi constant G_F, and the weak mixing angle $\sin^2\theta_W$. α is usually defined as a running parameter depending on the energy scale of the process, with $\alpha \approx 1/137$ at low energies, and $\alpha \approx 1/128$ at the energies close to M_Z. The definition of $\sin^2\theta_W$ depends on the renormalization convention. Throughout this thesis, we will use the "effective angle" $\sin^2\theta^{eff}_W$ for Z^0 coupling to electron, as described below.

2.2 $e^+e^- \longrightarrow Z^0 \longrightarrow f\bar{f}$ process

At a tree level, the $e^+e^- \longrightarrow Z^0 \longrightarrow f\bar{f}$ process cross section depends on the last term in the Lagrangian 2.6:

$$\mathcal{L} \sim \bar{\psi_f}\gamma^\mu(v_f - a_f\gamma^5)\psi_f Z_\mu \tag{2.8}$$

To emphasize the difference between the treatment of left-handed fermions $\psi_f^L = \frac{1}{2}(1-\gamma^5)\psi_f$ and right-handed fermions $\psi_f^R = \frac{1}{2}(1+\gamma^5)\psi_f$, this term can be rewritten as

$$\mathcal{L} \sim \bar{\psi_f^R}\gamma_\mu(v_f + a_f)\psi_f^L Z^\mu + \bar{\psi_f^L}\gamma_\mu(v_f - a_f)\psi_f^R Z^\mu \tag{2.9}$$

The coupling strength is apparently different for left- and right- handed fermions, and the cross section of the process is therefore expected to depend on the helicity states of the particles involved.

To interpret the results of e^+e- collider experiments, we need to define the electron (positron) beam polarization. We define the parameter $P(\hat{n})$ for a group of fermions and an arbitrary direction $\hat{n}$ as

$$P(\hat{n}) = \frac{N(spins\ parallel\ to\ \hat{n}) - N(spins\ antiparallel\ to\ \hat{n})}{N(spins\ parallel\ to\ \hat{n}) + N(spins\ antiparallel\ to\ \hat{n})} \tag{2.10}$$

where N is the number of fermions in the group that have the described spin direction. The polarization $\vec{\mathcal{P}}$ of the group is then defined as the vector in the direction of $\hat{s}$ with the magnitude of $P(\hat{s})$, where $\hat{s}$ is the direction along which the $P(\hat{s})$ is maximized. The longitudinal polarization of the beam $\mathcal{P}^z$ is defined as $P(\hat{z})$, where $\hat{z}$ is the direction of the beam momentum. The transverse polarization $\mathcal{P}^t$ is equal to $\sqrt{|\vec{\mathcal{P}}|^2 - (\mathcal{P}^z)^2}$. According to this definition, a right-handed beam has positive longitudinal polarization.

The polarized differential cross section of the $e^+e^- \longrightarrow Z^0 \longrightarrow f\bar{f}$ process is given (neglecting the fermion mass) by

$$\begin{aligned}\frac{d\sigma_f^Z}{d\Omega} = \; & \frac{N_c\alpha^2}{64\,\sin^4\theta_W\,\cos^4\theta_W}\,\frac{s}{(s-M_Z^2)^2 + s^2\Gamma_Z^2/M_Z^2}\times \\ & \times\{(1-\mathcal{P}_e^z\mathcal{P}_p^z)\left[(1+\cos^2\theta)(v_e^2+a_e^2)(v_f^2+a_f^2) + 8\cos\theta\, v_e a_e v_f a_f\right] \\ & +(\mathcal{P}_p^z - \mathcal{P}_e^z)\left[2(1+\cos^2\theta)v_e a_e(v_f^2+a_f^2) + 4\cos\theta\,(v_e^2+a_e^2)v_f a_f\right] \\ & +\mathcal{P}_e^t\mathcal{P}_p^t\cos(\phi_e+\phi_p)(1-\cos^2\theta)(v_e^2+a_e^2)(v_f^2+a_f^2)\}\end{aligned} \tag{2.11}$$

where $N_c = 1$ if f is a lepton, and $N_c = 3$ if f is a quark; $\mathcal{P}_e$ and $\mathcal{P}_p$ are the polarizations of the electron and the positron beams; θ is the polar angle of the outgoing fermion with respect to the incident electron direction; ϕ_e and ϕ_p are the azimuthal angles between the outgoing fermion and the incident beam polarization direction, for electrons and positrons respectively.

In the case of longitudinally polarized electrons and unpolarized positrons, which is relevant to the SLD experiment, the expression is simplified (from now on, we will omit the "z" superscript and use $\mathcal{P}_e$ notation for the electron longitudinal polarization):

$$\begin{aligned}\frac{d\sigma_f^Z}{d\Omega} = \; & \frac{N_c\alpha^2(v_e^2+a_e^2)(v_f^2+a_f^2)}{64\,\sin^4\theta_W\,\cos^4\theta_W}\,\frac{s}{(s-M_Z^2)^2+s^2\Gamma_Z^2/M_Z^2}\times \\ & [(1+\cos^2\theta)(1-\mathcal{P}_e A_e) + 2A_f\cos\theta(A_e - \mathcal{P}_e)]\end{aligned} \tag{2.12}$$

where we introduced the initial and the final state coupling parameters :

$$\begin{aligned} A_e &\equiv \frac{2v_e a_e}{v_e^2 + a_e^2} \\ A_f &\equiv \frac{2v_f a_f}{v_f^2 + a_f^2} \end{aligned} \tag{2.13}$$

Precise measurement of the parameters related to the absolute value of the Z^0 production cross section is complicated due to the uncertainties associated with the overall coefficient in the equation 2.12, and apparent sensitivity to the detector-related instrumental uncertainties, like the event selection efficiency and the detector acceptance. Therefore, it is often advantageous to measure left-right and forward-backward asymmetries of the final state fermion distributions instead.

The most precise $\sin^2\theta_W$ determination is performed by measuring the left-right asymmetry of Z^0 production in polarized e^+e^- collisions:

$$A_{LR} \equiv \frac{\sigma(e_L^- e^+ \to Z^0) - \sigma(e_R^- e^+ \to Z^0)}{\sigma(e_L^- e^+ \to Z^0) + \sigma(e_R^- e^+ \to Z^0)} \tag{2.14}$$

where the positron is unpolarized, e_L^- and e_R^- denote left- and right-handed electrons respectively. Since the sign of the electron beam polarization at the SLAC Linear Collider can be reversed, it is possible to measure the asymmetry in the number of Z^0 bosons created by left- and right-handed beams:

$$A_{LR}^{f,Measured} = \frac{\sigma_{[\mathcal{P}_e<0]}(e^- e^+ \to Z^0 \to f\bar{f}) - \sigma_{[\mathcal{P}_e>0]}(e^- e^+ \to Z^0 \to f\bar{f})}{\sigma_{[\mathcal{P}_e<0]}(e^- e^+ \to Z^0 \to f\bar{f}) + \sigma_{[\mathcal{P}_e>0]}(e^- e^+ \to Z^0 \to f\bar{f})} \tag{2.15}$$

The cross sections $\sigma_{[\mathcal{P}_e<0]}(e^-e^+ \to Z^0 \to f\bar{f})$ and $\sigma_{[\mathcal{P}_e>0]}(e^-e^+ \to Z^0 \to f\bar{f})$ can be calculated by integrating equation 2.12 over the range of $\cos\theta$ accepted by the detector. If the detector acceptance is symmetric in $\cos\theta$, as is the case with the SLD, the anti-symmetric term in $\cos\theta$ cancels out, and the integration yields

$$A_{LR}^{f,Measured}$$

$$= \frac{\int_{-c}^{+c}(1+\cos^2\theta)(1+|\mathcal{P}_e|A_e)\,d(\cos\theta) - \int_{-c}^{+c}(1+\cos^2\theta)(1-|\mathcal{P}_e|A_e)\,d(\cos\theta)}{\int_{-c}^{+c}(1+\cos^2\theta)(1+|\mathcal{P}_e|A_e)\,d(\cos\theta) + \int_{-c}^{+c}(1+\cos^2\theta)(1-|\mathcal{P}_e|A_e)\,d(\cos\theta)} \qquad (2.16)$$

$$= \frac{\int_{-c}^{+c}(1+\cos^2\theta)2|\mathcal{P}_e|A_e\,d(\cos\theta)}{\int_{-c}^{+c}(1+\cos^2\theta)2\,d(\cos\theta)} = |\mathcal{P}_e|A_e$$

The dependencies on the detector acceptance and the final state flavor have dropped out of the equation, which allows for a very precise measurement (in fact, the detection efficiency does not necessarily have to be symmetric in $\cos\theta$ to drop from the equation - since the only difference between left and right handed Z^0s, from the detection point of view, is that the distributions of outgoing fermions are reversed in the polar angle with respect to the electron beam direction, it is sufficient to have the detector acceptance and efficiency either symmetric in the polar angle, or equal for fermions and anti-fermions at any given polar angle. Both conditions are satisfied for the SLD detector).

The measured asymmetry is linear in the electron polarization, and provides a direct measure of the initial state coupling parameter A_e. Substituting expressions 2.13 for A_e

and 2.7 for the vector and axial couplings v_e and a_e, we obtain:

$$\frac{A_{LR}^{Measured}}{|\mathcal{P}_e|} = A_{LR} = A_e = \frac{2(1-4sin^2\theta_W)}{1+(1-4sin^2\theta_W)^2} \tag{2.17}$$

2.3 Total $e^+e^- \longrightarrow f\bar{f}$ cross section

While the Z-exchange dominates at the center-of-mass energies close to M_Z, two other processes contribute to the total $e^+e^- \longrightarrow f\bar{f}$ cross section, and must be taken into account in a precise measurement.

Pure γ-exchange tree-level cross section is given by

$$\frac{d\sigma_f^\gamma}{d\Omega} = N_c\frac{\alpha^2}{4s}q_f^2(1+\cos^2\theta) \tag{2.18}$$

At $\sqrt{s} = M_Z$, the contribution from the γ-exchange is about 800 times smaller than from the Z-exchange.

$Z-\gamma$ interference term is given, at a tree level, by

$$\begin{aligned}\frac{d\sigma_f^{[Z\gamma]}}{d\Omega} = \; & -2q_f\left(1-\frac{M_Z^2}{s}\right)\frac{N_c\alpha^2(v_e^2+a_e^2)(v_f^2+a_f^2)}{64\ \sin^4\theta_W\ \cos^4\theta_W}\times\frac{s}{(s-M_Z^2)^2+s^2\Gamma_Z^2/M_Z^2}\times \\ & \times\{(1+\cos^2\theta)v_ev_f+2\cos\theta\, a_ea_f-\mathcal{P}_e\left[(1+\cos^2\theta)v_fa_e+2\cos\theta\, v_ea_f\right]\}\end{aligned} \tag{2.19}$$

and disappears at $\sqrt{s} = M_Z$. However, no collider experiment takes place at exactly M_Z center-of-mass energy, due to both accelerator-related limitations, and energy smearing by the initial state radiation. As a result, $Z-\gamma$ interference may produce measurable contribution to the total Z^0 production cross section.

2.4 Radiative corrections and effective weak mixing angle

At the current level of experimental precision, tree level calculations are clearly insufficient for accurate comparison between theory and experiment, and at least full $\mathcal{O}(\alpha)$ radiative corrections must be applied. The radiative corrections to the $e^+e^- \longrightarrow f\bar{f}$ process can be divided into two categories (figure 2.1):

- External photon corrections - initial and final state radiation. The contributions from these corrections depend on energies, event selection criteria, etc., and are therefore experiment-specific.
- Virtual electroweak corrections - vacuum polarization diagrams, vertex corrections, boxes, etc.

To express our results in a form that is directly comparable to the results of other experimental groups and the Standard Electroweak Model calculations, we adopt the following convention. The measured value of A_{LR} is corrected to explicitly remove the effects of photon exchange, $Z-\gamma$ interference, external photon corrections, and the center-of-mass energy not being exactly equal to M_Z. The resulting corrected value A^0_{LR} absorbs the electroweak radiative corrections from the second group. Since these corrections involve summation over all heavy particles, A^0_{LR} is sensitive to the t-quark and the Higgs boson masses, as well as to possible existence of particles not included

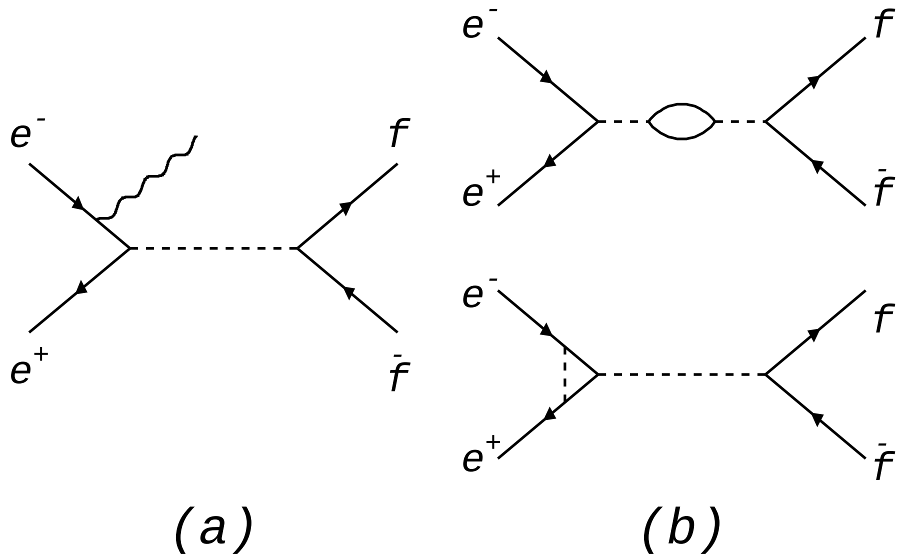

Figure 2.1: Examples of radiative corrections: (a) - external photon (b) - virtual (vacuum polarization and vertex).

in the minimal Standard Model. Ignoring negligible electroweak boxes, we modify the tree level expressions 2.7 for the vector and axial couplings to include contributions from vertex and vacuum polarization electroweak radiative corrections by introducing "effective" parameters $\sqrt{\rho_f}$ and $\sin^2\theta_W^{eff}$

$$\begin{aligned} \bar{v}_f &\equiv \sqrt{\rho_f}(t_f^3 - 2q_f \sin^2\theta_W^{eff}) \\ \bar{a}_f &\equiv \sqrt{\rho_f} t_f^3 \end{aligned} \tag{2.20}$$

and thus retaining the functional form of the tree level expression 2.17 for A_{LR}:

$$A_{LR}^0 \equiv \bar{A}_e \equiv \frac{2\bar{v}_e\bar{a}_e}{\bar{v}_e^2 + \bar{a}_e^2} \equiv \frac{2(1-4sin^2\theta_W^{eff})}{1+(1-4sin^2\theta_W^{eff})^2} \tag{2.21}$$

which becomes a definition of the effective weak mixing angle $\sin^2\theta_W^{eff}$.

The initial state radiation, which in this scheme must be taken into account explicitly, smears the center-of-mass energy of the reaction. If $\sigma_{tot}^0(s)$ is the combined cross section of Z-exchange, photon exchange, and $Z-\gamma$ interference at the center-of-mass energy s, the observed cross section $\sigma_{tot}(s)$ is obtained by convoluting $\sigma_{tot}^0(s)$ with the electron structure functions:

$$\sigma_{tot}(s) = \int D_e(x_1,s)D_e(x_2,s)\sigma_{tot}^0(x_1x_2s)\,dx_1dx_2 \tag{2.22}$$

where x_1 and x_2 are the momentum fractions carried by the electron and the positron after radiating, and the electron structure function $D_e(x,s)$ is given by [14]:

$$\begin{aligned} D_e(x,s) &= \beta(1-x)^{\beta-1}\left(1+\frac{3\beta}{4}\right) - \frac{\beta(1-x)}{2} \\ \text{where } \beta &= \frac{\alpha}{\pi}\left(\log\frac{s}{m_e^2}-1\right) \end{aligned} \tag{2.23}$$

The region of the integration over x_1 and x_2 is determined by the event selection cuts, and is often hard to determine precisely. For the A_{LR}^0 measurement, however, the cuts can be fairly relaxed because, as we have seen, there is no need to distinguish between different final states, and uncertainty in the integration region determination has a very small effect [15] on the measured A_{LR}^0 value. Calorimeter-based cuts on the total energy and the energy imbalance (see section 5.2) result in the following requirements:

$$\begin{aligned} & x_1 + x_2 < \frac{15}{40} \\ & \frac{|x_1 - x_2|}{x_1 + x_2} < 0.6 \end{aligned} \tag{2.24}$$

The integration was performed using the ZFITTER code [16], and cross checked by Monte-Carlo integration of the expression 2.22 over the region defined by 2.24, using tree-level expressions (with renormalized couplings) for all cross sections. The error in the A_{LR}^0 determination due to uncertainty in the integration boundary was estimated [15] to be approximately $5 \cdot 10^{-5}$ - a negligible effect compared to other sources of systematic errors.

In addition to smearing the center-of-mass energy, the initial state radiation affects the angular distribution of outgoing fermions. As a result, the measured left-right asymmetry has a small dependence on the acceptance of the detector, and the dependence on the polarization is not perfectly linear. Also, since the cross sections of the three concurrent processes (Z-exchange, γ-exchange, and $Z-\gamma$ interference) that contribute to the total $e^+e^- \longrightarrow f\bar{f}$ cross section depend differently on the final state fermion charges, the measured asymmetry is somewhat sensitive to the mixture of final state flavors accepted by the event selection criteria. In the SLD case, the Z^0 data sample consist almost entirely of hadronic events, with a very small contribution from $\tau^+\tau^-$ pairs. All these effects have been evaluated [15] and found to be negligible (the effect on the measured asymmetry was less than 10^{-4}).

2.5 Other electroweak asymmetries

Since the $e^+e^- \longrightarrow Z^0 \longrightarrow f\bar{f}$ cross section 2.12 has a term proportional to $\cos\theta$, the distribution of outgoing fermions is asymmetric between forward and backward (with respect to the incident electron direction) hemispheres even when the electrons are not polarized, which is the case for all e^+e^--collider experiments except the SLD. We define the forward-backward asymmetry as

$$A^f_{FB} \equiv \frac{\sigma_{[\cos\theta>0]}(e^+e^- \longrightarrow Z^0 \longrightarrow f\bar{f}) - \sigma_{[\cos\theta<0]}(e^+e^- \longrightarrow Z^0 \longrightarrow f\bar{f})}{\sigma_{[\cos\theta>0]}(e^+e^- \longrightarrow Z^0 \longrightarrow f\bar{f}) + \sigma_{[\cos\theta<0]}(e^+e^- \longrightarrow Z^0 \longrightarrow f\bar{f})} \qquad (2.25)$$

Substituting expression 2.12 with $\mathcal{P}_e = 0$ for the cross section and integrating over $\cos\theta$, we obtain:

$$A_{FB}^{f} = \frac{3}{4} A_e A_f \tag{2.26}$$

In a real experiment, however, the integration must be performed over the acceptance range of the detector, which does not drop from the final expression. Unlike A_{LR}, the measured value of A_{FB}^{f} is therefore sensitive to the detector acceptance, efficiency, and the final state flavor, which results in larger systematic uncertainty. Sensitivity to the effective electroweak mixing angle is lower than in the case of A_{LR}.

Other asymmetries that can be used to measure the $\sin^2\theta_W^{eff}$ include the double left-right forward-backward asymmetry

$$\tilde{A}_{FB}^{f} \equiv \frac{\sigma_{[\cos\theta>0,\mathcal{P}_e<0]} - \sigma_{[\cos\theta<0,\mathcal{P}_e<0]} - \sigma_{[\cos\theta>0,\mathcal{P}_e>0]} + \sigma_{[\cos\theta<0,\mathcal{P}_e>0]}}{\sigma_{[\cos\theta>0,\mathcal{P}_e<0]} + \sigma_{[\cos\theta<0,\mathcal{P}_e<0]} + \sigma_{[\cos\theta>0,\mathcal{P}_e>0]} + \sigma_{[\cos\theta<0,\mathcal{P}_e>0]}} = \frac{3}{4} |\mathcal{P}_e| A_f \tag{2.27}$$

and the final state fermion polarization asymmetry

$$P_f \equiv \frac{\sigma_{[\mathcal{P}_f<0]} - \sigma_{[\mathcal{P}_f>0]}}{\sigma_{[\mathcal{P}_f<0]} + \sigma_{[\mathcal{P}_f>0]}} = -A_f \tag{2.28}$$

Measuring P_f requires analyzing the final state fermion helicity and is practical for the case of $\tau^+\tau^-$ pair production where it can be extracted from the angular distribution of the outgoing τ-leptons. The P_τ measurement is statistically limited, however, due to low $Z^0 \longrightarrow \tau^+\tau^-$ branching ratio and generally low $\tau^+\tau^-$ pair detection efficiency.

Achieving low systematic error in the P_τ measurement is also difficult due to complicated analysis required for distinguishing between $\tau^+\tau^-$ and background events.

When P_τ is measured as a function of the outgoing fermion polar angle $\cos\theta$, it can also be used to extract A_l:

$$P_\tau = -\frac{A_\tau(1+\cos^2\theta) + 2A_e\cos\theta}{1+\cos^2\theta + 2A_eA_\tau\cos\theta} \tag{2.29}$$

In chapter 7, we will discuss the results of electroweak parameters measurements based on the asymmetries described in this section, performed by the SLD and the four LEP experiments: ALEPH, DELPHI, OPAL, and L3.

Chapter 3

Experimental apparatus

This chapter briefly describes the four major hardware components involved in the A^0_{LR} measurement: accelerator, detector, energy spectrometers, and polarimeter. Detailed description of the design, operation and analysis procedures for the QFC polarimeter can be found in Chapter 4.

3.1 SLAC Linear Collider

The SLAC Linear Collider (SLC) is the world's first and only linear collider that routinely operates with a polarized electron beam [17]. A schematic of the SLC is shown in figure 3.1.

Polarized electrons are produced by photoemission from a strained GaAs photocathode [18]. Two bunches of electrons (one for use in collisions, the other one for positron production) are injected into the Linear Accelerator (LINAC) and accelerated

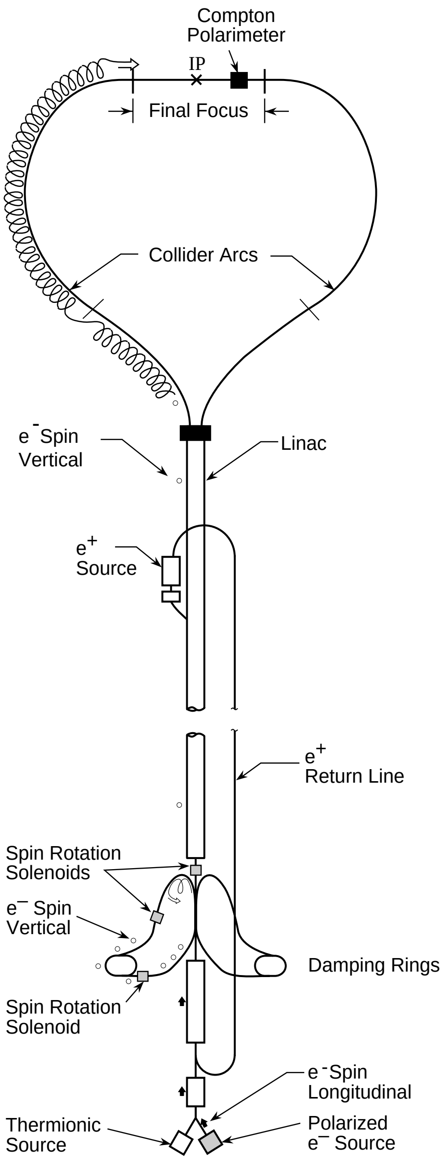

Figure 3.1: Polarized SLAC Linear Collider.

to 1.19 GeV, then pushed by a pulsed "kicker" magnet into the Linac-To-Ring transfer line (LTR) and transported to the electron damping ring. The electrons are kept in the damping ring for 8 ms to reduce the beam emittance, then transported back into the LINAC through the Ring-To-Linac transfer line (RTL). A positron bunch is extracted from the positron damping ring, and all three bunches, separated by about 60 ns, are accelerated in the LINAC. One of the electron bunches is accelerated to 30 GeV and sent to the positron production target. Positrons created at the target are accelerated to 200 MeV and transported back to the beginning of the LINAC and then to the positron damping ring, where they are stored for 16 ms. The remaining two bunches, one electron and one positron, proceed towards the end of the LINAC and reach an energy of 46.6 GeV before being deflected into the collider arcs. Electrons go into the north arc, and positrons go into the south arc. After losing about 1 GeV of their energy due to synchrotron radiation in the arcs, electrons and positrons go through the North and the South Final Focus respectively, and collide at the SLD interaction point (SLD IP). After the collision, unscattered electrons proceed to the South Final Focus where their polarization is analyzed by the Compton polarimeter. The energy of each beam is measured by the extraction line energy spectrometer. The repetition rate of the machine is 120 Hz.

The electron beam is longitudinally polarized at the source, and the polarization remains longitudinal until the beam is kicked into the LTR. In the LTR, the spin precesses by 450° and then rotates in the LTR spin rotator magnet to become vertical at the entry to the damping ring, so that the polarization is preserved during the storage and transport back to the LINAC. The polarization remains vertical until the electrons reach the end of the LINAC. The details of the spin transport through the collider arcs are too complicated to be reliably modeled. However, an experimental procedure has been developed to achieve longitudinal orientation at the SLD IP. The spin precession in each of the 23 achromats in the arc is 1085°, and the betatron phase advance is 1080°. Therefore, the SLC arcs operate near the spin tune resonance, and a pair of vertical betatron oscillations can be introduced to rotate the spin. The amplitudes of these oscillations are empirically adjusted to maximize the longitudinal polarization at the SLD IP measured by the Compton polarimeter.

3.2 WISRD energy spectrometers

The energies of the SLC beams are measured by the extraction line energy spectrometers called WISRDs. In each spectrometer, the beam goes through three dipole magnets. The central magnet is precisely calibrated, and its bending angle is used to determine the beam energy. Two other magnets bend the beam in a direction perpendicular to the bend direction of the central magnet in order to create two parallel stripes of synchrotron radiation, which are detected by wire arrays located in the beam focal point about 15 meters downstream of the analysis magnet. By measuring the distance between these two stripes, the deflection angle created by the central magnet can be determined. The difference in the widths of the two stripes provide a measure of the energy spread. The quoted precision of the WISRD, based on the original magnetic measurements done on the bench in 1986 [19] and on in situ surveys done once per every SLD run, results in an uncertainty on the measured center-of-mass energy E_{cm} of about 17 MeV [20] for a sufficiently large data sample where statistical errors can be neglected. Since the SLD detector is operated near the Z^0 resonance, and the Z^0 mass has been precisely measured by the LEP experiments [21], scanning the Z peak lineshape presents an excellent opportunity for checking the absolute calibration of the WISRD spectrometers. However, such a scan was not practical until 1997 due to the relatively low luminosity delivered by the SLC at that time - collecting sufficient off-peak statistics required spending unacceptably large amount of time for this experiment. The scan was done at the end of the SLD 1997/98 run when increased luminosity allowed for achieving the desired accuracy of about 20 MeV in less than a week. The peak scan data analysis and related issues are discussed below following the description given in [22].

The optimal scan that minimizes off-peak running time includes two off-peak points placed at +880 MeV and -930 MeV where the resonance curve is the steepest. Systematic uncertainties do not need to be explicitly accounted for unless they are different for different energy points. These can possibly include the purity and efficiency of the Z event selection, trigger efficiency, and the WISRD instrumental effects.

Two separate problems affecting the WISRD measurements have been discovered [23]: occasional abnormally high collected charge readings on the positron WISRD correlated with incorrect energy measurements, and occasional unphysically high energy width readings on the electron WISRD also correlated with incorrect energy measurements. The first effect was attributed to the collimator in front of the WISRD wire array that went out of position. The origin of the second effect is not precisely known but is believed to be related to the WISRD energy width determination algorithm working incorrectly when there are noisy wires at certain locations with respect to the synchrotron stripe. While both problems are noticeable only when the synchrotron stripes produced by the beams in the WISRD magnets are at specific rather uncommon positions in the wire arrays and therefore affect only small portion of the SLD data, both are present in the off-peak data sample. The corrections to the measured center-of-mass energy caused by these effects and associated systematic errors have been estimated [22] and are listed in table 3.1 along with other corrections applied to the Z-peak scan data before fitting it with the Z lineshape.

A measure of the relative cross section for each of the scan points is provided by the ratio of the Z^0 production rate and the Bhabha event rate as measured by the luminosity monitors. The numbers of Zs and Bhabhas detected for each scan point are listed in table 3.1 along with the trigger inefficiencies ϵ calculated [22] as a fraction of machine pulses when the trigger or the data acquisition systems were not ready to accept events. To correct for these inefficiencies, the observed Z/Bhabha ratio should be multiplied by $1/(1-\epsilon)$. In order to minimize the trigger related effects, purely calorimetric Z^0 event selection algorithm known as KAL [24] was used for the analysis instead of the tracking assisted procedure described in this thesis. The associated impurity level is about 0.3 %.

Table 3.1: Z-peak scan data.

	Low energy point	Peak	High energy point
Intended energy setpoint	90.352 GeV	91.284 GeV	92.167 GeV
Uncorrected energy measured by WISRD	90.236 GeV	91.176 GeV	92.048 GeV
Positron WISRD correction	-13.4 ± 6.7 MeV	-0.3 ± 0.2 MeV	0
Electron WISRD correction	-20.9 ± 10.5 MeV	-4.9 ± 2.5 MeV	$+3.0 \pm 1.5$ MeV
SLD IP to WISRD energy loss	$+36.9 \pm 1.0$ MeV per beam	$+36.9 \pm 1.0$ MeV per beam	$+36.9 \pm 1.0$ MeV per beam
Beam-beam disruption correction	$+33.4 \pm 10.0$ MeV	$+32.5 \pm 10.0$ MeV	$+28.1 \pm 15.0$ MeV
Corrected energy measured by WISRD	90.309 ± 0.016 GeV	91.277 ± 0.010 GeV	92.153 ± 0.015 GeV
Z events	3,312	52,123	3,724
Bhabha events	12,621	122,850	11,174
Trigger inefficiency	0.030	0.023	0.033

The Bhabha event selection is background free at this level.

Two methods were used to fit the scan data - one using the ZFITTER program [16], and the other using the BHK program [25] to calculate the Bhabha cross section and a fitting function from Kuraev and Fadin [14]. The methods yielded Z mass values of 91.230 ± 0.025 GeV and 91.226 ± 0.025 GeV respectively, with χ^2 of 1.2 and 1.5 (both fits have one degree of freedom). Splitting the difference between these two results and inflating the error accordingly, we obtain the WISRD measured value for the Z mass equal to 91.228 ± 0.025 GeV. Compared to the LEP result of 91.1867 ± 0.0021 GeV, this represents an offset of -41 ± 25 MeV in the WISRD energy scale.

There is an independent way to determine the energies of the off-peak scan points using the Beam Profile Monitors (BPM) rather than WISRDs. BPMs are not precisely calibrated so the absolute scale is still set by the WISRD on-peak energy measurement. This analysis was done by Pantaleo Raimondi and produced slightly different (but comfortably consistent, within errors) values of $E_{cm}^{low} = 90.317$ GeV, $E_{cm}^{peak} = 91.277$ GeV, $E_{cm}^{high} = 92.168$ GeV. Using identical fitting procedure, these values yield the WISRD scale offset of -50 ± 22 MeV. Combining the WISRD and BPM based offsets and assigning an additional systematic error equal to one half of the difference between them, we obtain our final correction to the WISRD energy scale of -46 ± 25 MeV.

In order to calculate the average energy for the Z^0 data sample used for the A_{LR} analysis, we first compute the luminosity weighted average as measured by the WISRD, then apply the same types of correction that we applied to the peak scan data - WISRD instrumental errors, energy loss between the SLD IP and the WISRDs, energy loss due to beamstrahlung. The result is corrected for the WISRD scale offset determined by the Z peak scan as described above. The luminosity weighted corrections and the resulting average energies for the 1997 and 1998 SLD data samples are listed in table 3.2. The IP-to-WISRD energy loss was lower in 1998 because a different beam configuration was used with the strength of one of the dipole magnets decreased and off-axis beam positioning in quadrupoles being used to provide additional bending angle. Given that the origin of the energy scale miscalibration is not precisely known and is possibly related to the beam-beam disruption effects caused by the high luminosity observed during the most recent SLD run, we decided to apply the Z peak scan based energy scale correction only to the 1997-98 data (which is about 70 % of our data sample). The luminosity-weighted average center-of-mass energies measured for all SLD runs are listed in table 3.3.

3.3 SLD detector

The products of the e^+e^- collisions are detected and analyzed by the SLC Large Detector (SLD). A cross section view of a quadrant of the detector is shown in figure 3.2. The SLD design [26] is typical for a collider detector, but is optimized to take full advantage of the SLC unique capabilities, such as the very small size of the interaction region that allows for precise vertexing.

Charged particle tracking is provided by the drift chamber [27] system and the vertex detector [28] operating in a uniform axial magnetic field of 0.6 T. About 70 % of the

Table 3.2: Luminosity weighted corrections and average center-of-mass energies for the SLD 1997 and 1998 Z data samples.

	1997	1998
WISRD instrumental correction	1 ± 1 MeV	4 ± 2 MeV
SLD IP to WISRD energy loss correction	$+41.9 \pm 1.0$ MeV per beam	$+36.9 \pm 1.0$ MeV per beam
Beam-beam disruption correction	$+22.3 \pm 10.0$ MeV	$+30.4 \pm 10.0$ MeV
Average energy after instrumental corrections	91.277 ± 0.010 GeV	91.286 ± 0.010 GeV
WISRD scale correction (based on Z-peak scan results)	-46 ± 25 MeV	-46 ± 25 MeV
Final average energy	91.231 ± 0.027 GeV	91.240 ± 0.027 GeV

Table 3.3: Luminosity-weighted average center-of-mass energies for all SLD runs.

1992	91.55 ± 0.04 GeV
1993	91.26 ± 0.02 GeV
1994/95	91.28 ± 0.03 GeV
1996	91.26 ± 0.03 GeV
1997/98	91.237 ± 0.027 GeV

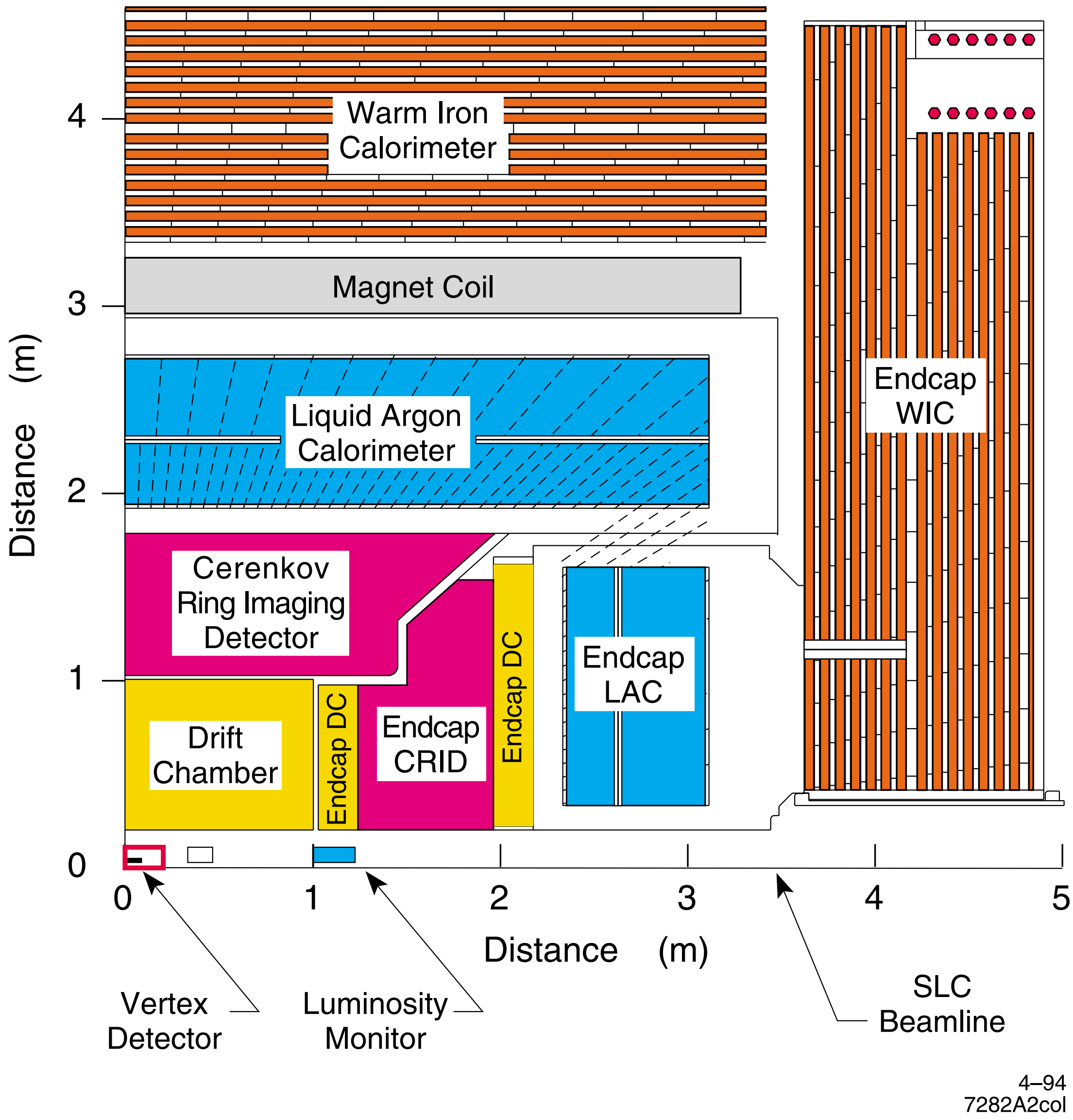

Figure 3.2: The SLD detector.

Z^0 events recorded by the SLD have been collected with an upgraded version of the vertex detector that comprises 96 two-dimensional charge-coupled devices (CCDs) with a total of 307 million pixels. The liquid argon calorimeter [29] is used primarily for triggering and event selection, and the Warm Iron Calorimeter [30] is used for muon identification. Additional powerful particle identification capabilities are provided by the Čerenkov ring imaging detector [31].

It should be noted, however, that only few of the SLD detector capabilities are actually utilized in the A^0_{LR} analysis. The power, robustness, and very low systematic error of the A^0_{LR} measurement described in this thesis comes from the fact that there is no need to distinguish between different hadronic final states of the Z^0 decays, and the detector acceptance has no effect on the measured left-right asymmetry, as discussed in section 2.2.

3.4 Compton polarimeter

The polarization of the electron beam is analyzed by the Compton polarimeter located in the SLC South Final Focus approximately 30 meters downstream from the SLD IP (figure 3.1). The schematics of the polarimeter is shown in figure 3.3. The electron beam is scattered off circularly polarized laser light at a point called the Compton interaction point (Compton IP). Since there are no dipole magnets between the SLD IP and the Compton IP, the polarization is preserved between these two points to first order (small corrections associated with the beam transport and chromaticity effects are

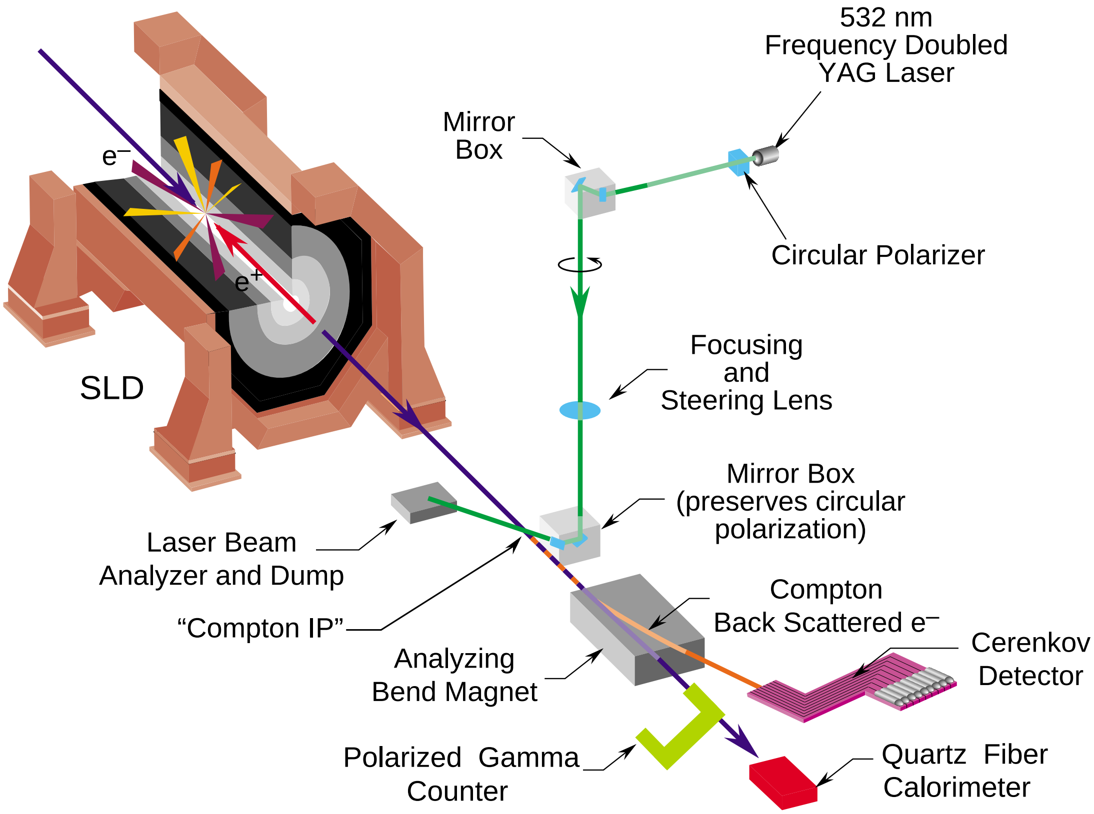

Figure 3.3: Compton polarimeter.

discussed later). The laser fires on every seventh machine pulse, and the signs of both the laser and the electron beam polarizations are changed randomly on a pulse-by-pulse basis. Compton scattered electrons are analyzed by a spectrometer consisting of two dipole magnets, and detected by the Čerenkov multichannel detector (CKV). The CKV is used to continuously monitor the polarization during the SLD physics data collection. Compton scattered photons are detected by two additional polarimeters, the Polarized Gamma Counter (PGC) and the Quartz Fiber Calorimeter (QFC). These two detectors are used to cross check the measurement by the CKV.

In the remainder of this section, we will briefly describe the Compton scattering basics, the polarimeter components, and present the results of the polarization measurement for the SLD data sample used for the A^0_{LR} analysis. Detailed discussion of the QFC polarimeter is postponed until chapter 4.

3.4.1 Compton scattering cross section and kinematics

The spin dependence of the Compton scattering cross section has been used on many occasions for measuring electron beam polarization. This section lists some general formulae describing the cross section, and then discusses the SLD Compton system.

To the lowest order, Compton scattering is described by the two Feynman diagrams corresponding to s- and u- channels. In the electron rest frame, the differential cross section is given by

$$\left(\frac{d\sigma}{d\Omega}\right) = \frac{1}{2}r_0^2\frac{k'}{k}\left(\frac{(k-k')^2}{kk'} + 1 + \cos^2\theta_0\right)(1 - P_\gamma P_e A_{e\gamma}(\vec{k}, \vec{k'})) \tag{3.1}$$

where r_0 is the classical radius of the electron, $\vec{k}$ and $\vec{k'}$ are the momenta of the incident and scattered photons, θ_0 is the photon scattering angle. P_e is the polarization of the electron, P_γ is the circular polarization of the photon. We use the convention where polarization is positive when the angular momentum is aligned with the momentum of the particle. Such states are called right-handed, or positive helicity states, and quantities corresponding to these states are labeled by "R". The states where angular momentum and momentum of the particle are anti-parallel are called left-handed, or negative helicity states, and are labeled by "L". The asymmetry function $A_{e\gamma}$ is given by

$$A_{e\gamma}(\vec{k}, \vec{k'}) = \frac{(\frac{1}{k'} - \frac{1}{k})(\vec{k}\cos\theta_0 + \vec{k'})\hat{s}}{\frac{(k-k')^2}{kk'} + 1 + \cos^2\theta_0} \tag{3.2}$$

where $\hat{s}$ is the electron spin direction. Therefore, it is possible to use Compton scattering to analyze both longitudinal and transverse components of the electron beam polarization.

In order to apply the above relations to the analysis, we have to rewrite them in the laboratory frame where, in case of the SLD Compton system, we have an essentially head-on (10 milliradians crossing angle) collision between a 45.6 GeV electron and a 2.33 eV photon. We define E and K to be the incident energies of the electron and the photon in this frame, and E' and K' to be their energies after the scattering. It is convenient to introduce two new variables x and y given by

$$y \equiv \left(1 + \frac{4KE}{m^2}\right)^{-1} \tag{3.3}$$

$$x \equiv \frac{1 - \cos\theta_0}{2y + (1+y)(1 - \cos\theta_0)} \tag{3.4}$$

where m is the electron mass. y is the ratio of the minimal possible energy of the scattered electron to the energy of the incident electron, and x is the ratio of the scattered photon energy to the maximum possible scattered photon energy. Therefore,

$$K'_{max} = E(1-y) + K \tag{3.5}$$

and the relation between the scattered photon energy and its angle θ with respect to the direction of the incident electron is described by

$$K' = K'_{max}\left[1 + y\left(\frac{E\theta}{m}\right)^2\right]^{-1} = xK'_{max} \tag{3.6}$$

The differential cross section given by 3.1 and 3.2 in the electron rest frame can be written in the laboratory frame as

$$\left(\frac{d^2\sigma}{dx\,d\phi}\right)_{Comp} = \left(\frac{d^2\sigma}{dx\,d\phi}\right)_{unpol}\left(1 - P_\gamma[P_e^z A_{e\gamma}^z(x) + P_e^t \cos\phi A_{e\gamma}^t(x)]\right) \tag{3.7}$$

where the superscripts z and t refer respectively to the longitudinal and the transverse components of the electron beam polarization, and ϕ is the azimuthal angle of the scattered photon with respect to the transverse component. The unpolarized cross section is given by

$$\left(\frac{d^2\sigma}{dx\,d\phi}\right)_{unpol} = r_0^2 y \left(\frac{x^2(1-y)^2}{1-x(1-y)} + 1 + \left(\frac{1-x(1+y)}{1-x(1-y)}\right)^2\right) \tag{3.8}$$

and the longitudinal and the transverse asymmetries are given by

$$A^z_{e\gamma} = r_0^2 y[1-x(1+y)]\left(1-\frac{1}{[1-x(1-y)]^2}\right)\left(\frac{d^2\sigma}{dx\,d\phi}\right)^{-1}_{unpol} \tag{3.9}$$

$$A^t_{e\gamma} = r_0^2 yx(1-y)\left(\frac{2\sqrt{xy(1-x)}}{1-x(1-y)}\right)\left(\frac{d^2\sigma}{dx\,d\phi}\right)^{-1}_{unpol} \tag{3.10}$$

The major parameters of the SLD Compton system are listed in table 3.4. Figure 3.4 shows the asymmetries described by 3.9 and 3.10 as a function of the kinematic variable x. Figure 3.5 shows the Compton scattering cross section as a function of x for unpolarized and 100 % longitudinally polarized electrons.

Because the momentum of the incident electron is 10 orders of magnitude higher than the momentum of the incident photon, the event are boosted in the forward direction in the laboratory frame, producing very narrow angular distributions of the scattered electrons and photons. Figure 3.6 shows transverse profiles of the energy flow in the beam of scattered Compton photons at the position of the QFC detector, for the two

Table 3.4: Major parameters of the SLD Compton system.

Incident electron energy (E)	45.60 GeV
Electron beam rate	120 Hz
Electron beam intensity	$3.5 * 10^{10}$ e^- per bunch
Electron beam size at the Compton IP, horizontal	530 μm
Electron beam size at the Compton IP, vertical	200 μm
Electron beam angular convergence at Compton IP, horizontal	80 μrad
Electron beam angular convergence at Compton IP, vertical	25 μrad
Laser wavelength	532 nm
Incident photon energy (K)	2.33 eV
Laser repetition rate	17 Hz
Laser beam / Electron beam crossing angle	10 mrad
Average number of Compton photons produced per electron bunch	1000
Maximum scattered photon energy (K'_{max})	28.25 GeV
Minimum scattered electron energy (E'_{min})	17.35 GeV
Asymmetry in the energy carried by the scattered photons, calculated between the parallel and anti-parallel combinations of the electron and the photon helicities (for longitudinally polarized electron beam)	0.17332
Distance between the Compton IP and the QFC detector	11.62 m

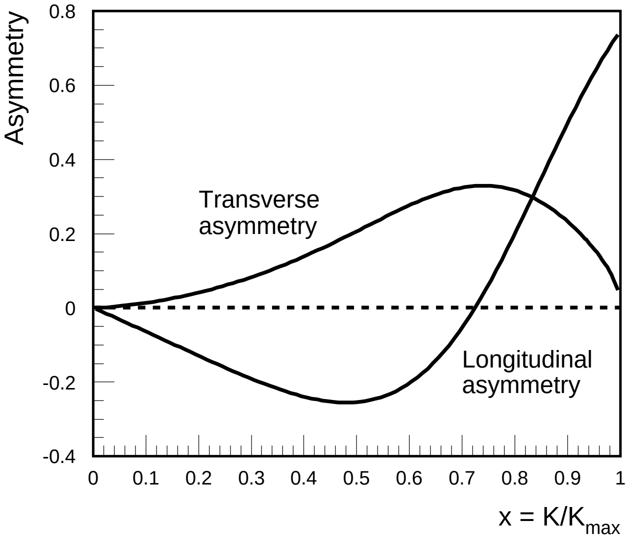

Figure 3.4: Compton asymmetries as a function of kinematic variable $x = K/K_{max}$. For the SLD Compton system, the maximum scattered photon energy $K_{max} = 28.25GeV$.

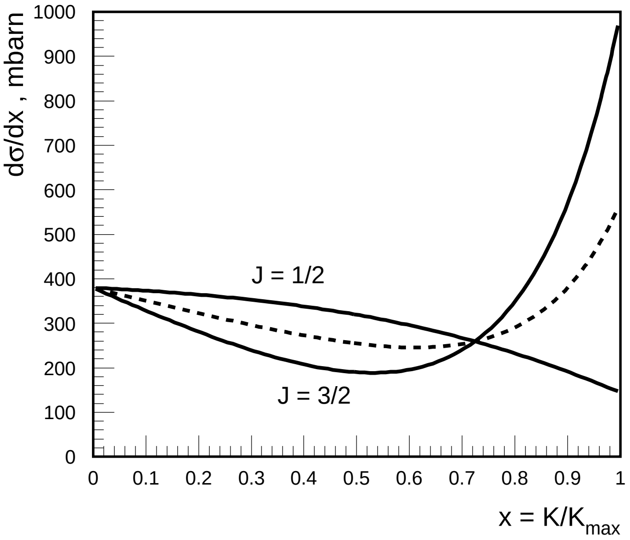

Figure 3.5: Polarized Compton cross section as a function of kinematic variable $x = K/K_{max}$. The electron is 100 % longitudinally polarized, the photon is 100 % circularly polarized. The $J = 3/2$ curve corresponds to the case of parallel, and the $J = 1/2$ curve to the case of anti-parallel combination of the electron and the photon helicities.

possible sign combinations of the electron and the photon polarizations, assuming 100 % longitudinal polarization of the electron beam. Finally, figure 3.7 shows the same profile for a 100 % transversely polarized electron beam.

Higher order corrections to the Compton cross section have been estimated [32], and their effect on the integrated asymmetry was found to be less than 0.1 %. Therefore, these corrections are ignored in the analysis described here.

3.4.2 Laser system

The photon beam is produced by a pulsed Nd:YAG laser (Spectra Physics GCR130) frequency doubled to 532 nm. After being polarized, the beam is transported down the ventilation shaft to the SLC South Final Focus and directed for head-on (10 milliradians crossing angle) collisions with the electron beam.

The laser beam is polarized with a linear polarizer and a pair of Pockels cells. The linear polarizer and the second of the two Pockels cells (PS cell) have their axes aligned, while the first Pockels cell (CP cell) axes are rotated by 45°. This setup allows for achieving an arbitrary elliptical polarization. Therefore, adjusting the Pockels cells voltages can be used to compensate for phase shifts introduced by other transport line elements (mirrors, lenses, windows, etc.) and to achieve circular polarization at the Compton IP. The polarization is measured before and after the IP, and modeling of the optic elements is used to extract the polarization at the Compton IP. Detailed description of the laser system and the laser beam polarization analysis for the SLD 1993 run can be found in [33]. Modifications made to the system and analysis procedures

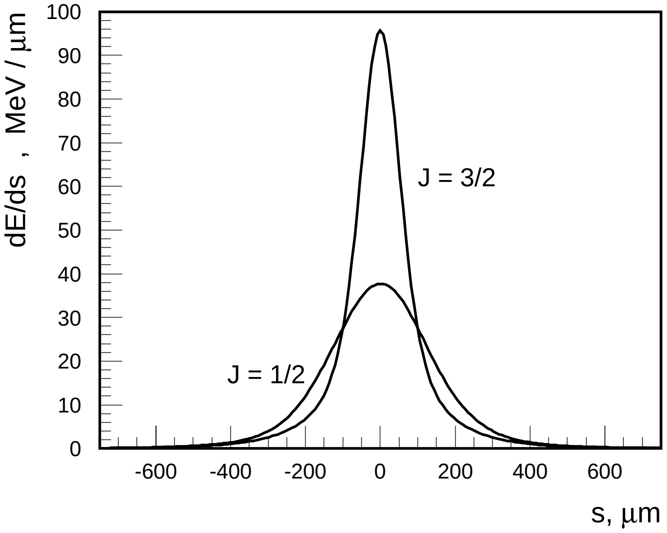

Figure 3.6: Compton energy profile at the entry to the QFC detector, for a longitudinally polarized point-like beam. The $J = 3/2$ curve corresponds to the case of parallel, and the $J = 1/2$ curve to the case of anti-parallel combination of the electron and the photon helicities.

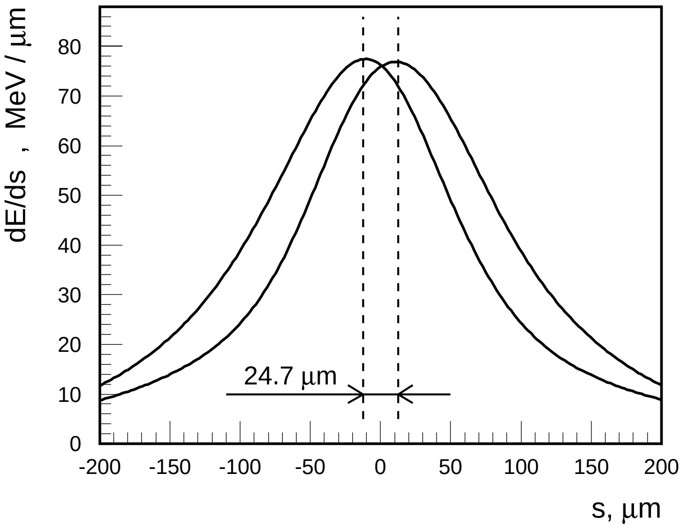

Figure 3.7: Compton energy profile at the entry to the QFC detector, along the direction of the transverse polarization, for a 100 % transversely polarized point-like beam. The two curves correspond to the two possible electron and photon polarization sign combinations.

used for the subsequent runs are described in [34] for the 1994/95, [35] for the 1996, and [36] for the 1997/98 SLD runs.

The laser is fired on every 7th SLC pulse. In order to avoid accidental synchronization with any machine related instabilities of the electron beam [37], the laser fires on the 6th rather than on the 7th pulse every 7 seconds.

3.4.3 Čerenkov electron spectrometer

The Čerenkov detector (CKV) detects Compton scattered electrons after they pass through a pair of analyzing dipole magnets. The CKV design [1] is shown in figure 3.8. It is a 9 channel Čerenkov gas counter with a lead preradiator. The transverse dimension of each channel is 1 cm by 1 cm. The CKV is mounted on a remotely operated table that allows for horizontal motion of the detector in the direction perpendicular to the direction of the electron beam. Table scans are done once a day in order to cross calibrate the channel gains and establish the position of the Compton edge (corresponding to the largest possible deflection angle of scattered electrons). In between these scans, the ratio of the signals in the two channels closest to the Compton edge is used to monitor the edge location (and therefore the analyzing power of each channel). Detailed description of the CKV data analysis procedures can be found in [38].

In reality, only channel 7, which is located close to the kinematic edge of the Compton spectrum, is used for calculating the polarization since it is least sensitive to systematic effects associated with the spectrometer calibration. However, other channels are very useful for the detector calibration, cross checks, and study of systematic uncertainties.

3.4.4 Cross check polarimeters

Since accurate polarization measurement is critical for the SLD physics program, and for the A^0_{LR} analysis in particular, cross check of the measurement provided by the CKV detector is highly desirable. To perform this cross check, two additional detectors have been constructed: the Polarized Gamma Counter (PGC) and the Quartz Fiber Calorimeter (QFC).

Both detect Compton scattered photons and are therefore completely insensitive to the magnetic spectrometer calibration. They do not share any systematics with the CKV detector other than the error in the laser polarization, which is understood at 0.1 % level. The detectors are complimentary to each other, with their potential sources of systematic errors being almost completely uncorrelated. PGC is a Čerenkov gas counter (figure 3.9) with three removable lead preradiators (1 in, 1 in, 0.5 in). Due to its high Čerenkov threshold, the PGC is insensitive to low energy beam related background, which is a serious problem for the QFC. Varying the total preradiator thickness allows for for a powerful way to cross check its Monte Carlo based analyzing power calibration. The QFC, on the other hand, is a total absorption calorimeter, and its analyzing power is therefore very close to the asymmetry in the energy carried by the Compton photons. Unlike both CKV and PGC, the QFC does not rely heavily on Monte Carlo simulation for the analyzing power calibration, and is unaffected, to the first order, by angular and position misalignments.

Both PGC and QFC can be operated only when the SLC beams are not in collision

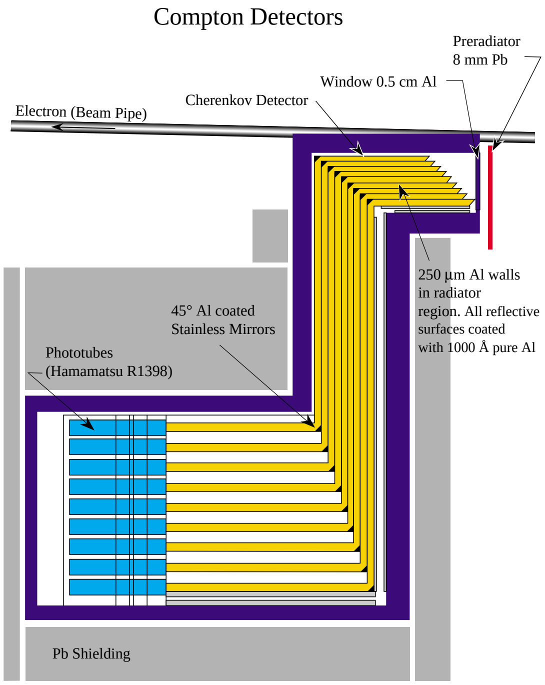

Figure 3.8: Čerenkov detector.

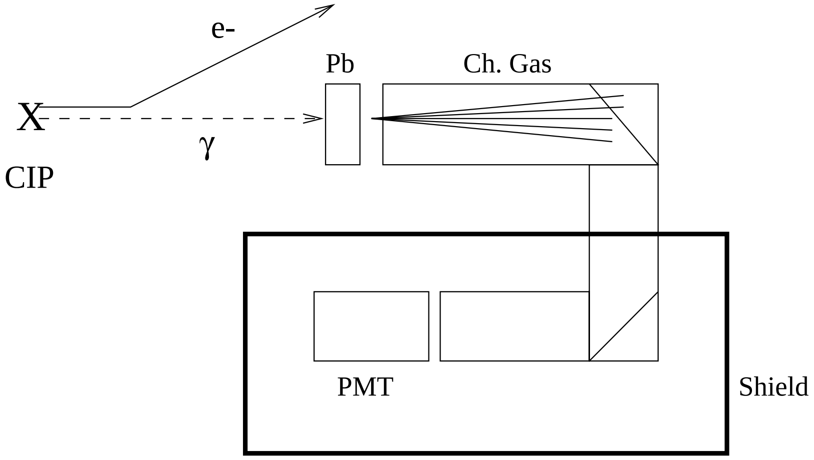

Figure 3.9: Polarized Gamma Counter.

(otherwise, they are overwhelmed by the beamstrahlung related background). During the SLD 1997/98 run, dedicated studies were performed to compare the polarization measurements by the CKV and the PGC, and by the CKV and the QFC (PGC and QFC cannot be used simultaneously since the PGC preradiator must be moved away from the beam in order for the QFC to be operational). The relative deviations of the polarizations measured with the cross check polarimeters from the polarizations measured by the CKV channel 7 (which was used in the physics analysis) for the same data samples were found to be $(+0.65 \pm 0.72)$ % and (-0.35 ± 0.64) % for the QFC and the PGC respectively. The measurements by all three detectors are clearly mutually consistent.

These results, along with comparison between the CKV channels 6 and 7, were used to estimate the systematic uncertainty of the polarization measurement by the SLD, as described later in this chapter.

Description of the PGC detector and related data analysis procedures can be found in [39]. The QFC polarimeter is discussed in detail in chapter 4.

3.4.5 SLD IP to Compton IP corrections

What is actually measured by the Compton polarimeter is the average longitudinal polarization at the Compton IP, which, in general, can be different from the luminosity-weighted average polarization at the SLD IP relevant to the A^0_{LR} analysis. The difference is caused by three factors: beam transport effects, depolarization by collisions, and the so-called chromaticity effect. These factors are briefly described below, and references to publications containing more detailed descriptions are given. Corrections to the measured polarization caused by each of these factors are summarized in table 3.5 for each of the SLD runs along with corresponding uncertainties.

Beam transport effects

Since there are no dipole magnets in the region separating the SLD and the Compton IP, no spin rotation is expected to occur as long as the beam is transported on the axis of the quadrupole lattice. The amount of residual beam steering introduced by quadrupoles was studied by P. Raimondi[40] and P. Emma[41] who concluded that the total beam rotation between the SLD IP and the Compton IP was less than 30 μrad in the horizontal and less than 50 μrad in the vertical directions. The resulting spin rotation is larger by a factor of $\gamma(g-2)/2 = 103.6$, still yielding a negligible difference in longitudinal polarizations at the SLD and the Compton IP (less than $2 * 10^{-5}$).

However, a non-negligible difference results from the fact that the longitudinal polarization of the beam is maximized (using the so-called spin bumps technique) at the Compton IP where the beam has much smaller angular divergence than at the SLD IP. The size of the effect on the polarization is given by [38]

$$\frac{P_{SLD}}{P_{Compton}} - 1 \approx -\frac{1}{2}\left[(\sigma'_x)^2 + (\sigma'_y)^2\right] \tag{3.11}$$

for a Gaussian beam with angular divergence $\sigma'_x\dot{\sigma}'_y$ at the SLD IP (the divergence at the Compton IT is negligible compared to it). Since the effective angular divergence can be

Table 3.5: Summary of SLD IP to Compton IP corrections to the measured beam polarization. Luminosity weighted polarization at the SLD IP is calculated as $P_{SLD} = P_{Compton}(1+\epsilon)$, where $P_{Compton}$ is the polarization measured by the polarimeter at the Compton IP, and ϵ is the correction listed in this table.

Run	Beam transport	Depolarization in collisions	Chromaticity	Total
1992				0 ± 0.002
1993	-0.00112 ± 0.00012	0 ± 0.001	$+0.017 \pm 0.011$	$+0.016 \pm 0.011$
1994/95	-0.00112 ± 0.00012	0 ± 0.001	$+0.0020 \pm 0.0014$	$+0.0009 \pm 0.0017$
1996	-0.0011 ± 0.0005	0 ± 0.001	$+0.0012 \pm 0.0012$	$+0.0002 \pm 0.0016$
1997/98	-0.0024 ± 0.0008	0 ± 0.001	$+0.0012 \pm 0.0008$	-0.0012 ± 0.0015

increased by pulse-to-pulse jitter in the direction of the incident beam, equation 3.11 was evaluated both for no jitter and for maximum observed jitter situations, and the average was used as a correction to the measured polarization, with half of the difference between the two numbers taken as an error. The biggest effect was observed during the 1997/98 run due to larger focusing angles being used at that time at the SLD IP.

Depolarization by collisions

Depolarization by collisions is expected to be negligible [42]. It was studied experimentally by comparing the polarimeter data taken with and without collisions, and was found to be consistent with zero (0.000 ± 0.001).

Chromaticity effect

Chromaticity effect is caused by the difference between the unweighted averaged polarization

$$P_{av} = \frac{\int n(E)P(E)dE}{\int n(E)dE} \tag{3.12}$$

measured by the polarimeter, and the luminosity weighted average polarization

$$P_{lum} = \frac{\int n(E)P(E)L(E)dE}{\int n(E)L(E)dE} \tag{3.13}$$

needed for the A^0_{LR} analysis (off-energy electrons in the beam tails are poorly focused at the SLD IP and therefore produce little luminosity, but they still contribute to the measured polarization). $n(E)$ is the beam energy distribution, $P(E)$ is the polarization dependence on the energy, and $L(E)$ is the luminosity as a function of the electron energy.

The beam energy distribution $n(E)$ was monitored with wire scans performed automatically every few hours.

When tuning the accelerator arc setup to achieve longitudinal polarization at the SLD IP, care was taken to make the polarization dependence on the energy as flat as possible by minimizing the effective number of spin turns in the arc. $P(E)$ was measured several times during each SLD run (at regular intervals, and after any significant changes to the arc setup) by varying the energy of the beam injected in the arc and looking at the effect on the polarization.

The luminosity dependence on the electron energy was studied [38, 42] using three different methods: semi-analytic model, numerical modeling (TURTLE simulation), and a direct estimation from the data. The level of consistency between the results produced by these methods was used to estimate the uncertainty in the $L(E)$ determination.

3.4.6 Luminosity weighted average polarization

Under normal running conditions, the Compton polarimeter produces a polarization measurement with statistical accuracy of approximately 1 % for every 3 minute time period. In order to determine the luminosity weighted polarization required for calculating A_{LR} (equation 6.1), each Z^0 event recorded by the SLD is associated with a particular value of the beam polarization measured close in time to the moment of the event. The luminosity weighted polarization for the data sample is then given by the average of the polarization values associated with individual events in the sample.

3.4.7 Results

Table 3.6 provides a summary of the average luminosity weighted polarization values for each of the SLD runs, along with associated systematic uncertainties.

The CKV polarimeter channel 7 (the channel closest to the Compton edge and therefore least sensitive to calibration errors) was used to determine the central value of the polarization.

For the first three SLD runs, the uncertainty in its analyzing power calibration was calculated by combining the estimated size of the CKV intrinsic uncertainties [38] with the size of the observed discrepancy between the CKV channels 6 and 7 (for the 1994/95 run, this discrepancy was very small).

Since 1996, a comparison with the QFC, the PGC, and the CKV channel 6 was used to estimate this uncertainty. The relative differences between the polarization values measured by these cross check detectors and by the CKV channel 7 were found to be $(+0.65 \pm 0.72)$ % for the QFC, (-0.35 ± 0.64) % for the PGC, and $(+0.68 \pm 0.65)$ % for the CKV channel 6. The weighted average of the relative deviations from the CKV channel 7 is (0.30 ± 0.39) % ($\chi^2 = 1.9$, 2 degrees of freedom), which leads us to quote a calibration uncertainty of 0.4 %.

Statistical errors are negligible.

Table 3.6: Luminosity weighted average polarization values and associated uncertainties for all SLD runs.

	1992	**1993**	**1994/95**	**1996**	**1997/98**
Relative systematic errors, per cent					
Laser Polarization	2.0	1.0	0.20	0.10	0.10
Detector Linearity	1.5	0.6	0.50	0.20	0.20
Analyzing Power Calibration	1.0	0.6	0.29	0.40	0.40
Electronic noise	0.4	0.2	0.20	0.20	0.20
SLD IP to Compton IP Correction Uncertainty	0.2	1.1	0.17	0.16	0.15
Total	**2.7**	**1.7**	**0.67**	**0.52**	**0.52**
Luminosity weighted average polarization					
	0.224 ± 0.006	**0.630 ± 0.011**	**0.7723 ± 0.0052**	**0.7616 ± 0.0040**	**0.7292 ± 0.0038**

Chapter 4

Polarization measurement with the Quartz Fiber Calorimeter

4.1 Detector design

4.1.1 Requirements to the detector. Choice of technology.

Designing a calorimeter-based photon detector capable of operating in the SLD environment proved to be a challenging task. To perform precise polarization measurement, the calorimeter has to satisfy the following set of requirements:

- Compactness. Very limited space is available for the detector, and the separation between the neutral beam line along which the Compton photons are traveling, and the beam pipe flanges, is only 10 mm.

- High position sensitivity. The spatial separation between the centroids of the Compton photon beams produces with different sign combinations of the photon and the electron polarizations is about 24.7μm for a 100 % transversely polarized electron beam.

- Radiation hardness. When the electron and the positron beams are in collision, the calorimeter serves as a beam dump for a high flux of beamstrahlung. We estimated that the lifetime dose for the detector could be as high as 8 GRad.

- Insensitivity to soft synchrotron radiation. The Soft Bend dipole magnet located between the Compton IP and the calorimeter generates about 460 TeV of synchrotron radiation per machine pulse, with a critical energy of 53.2 keV. This should be compared to about 15 TeV per pulse carried by the Compton photons. These synchrotron photons are not separated in space from the Compton beam, hence there is no way to prevent them from hitting the detector.

- High linearity is critical for a precise polarization measurement. This means, among other things, that the calorimeter should fully contain even the most energetic showers (Compton photons energies range from 0 to 28.25 GeV). Full containment is also important in order to avoid creating asymmetric background for other detectors located in the polarimeter area.

To satisfy these requirements, we decided to use a combination of a classic "sandwich" design, quartz fiber technology, and tungsten absorber.

Using tungsten allows for a compact "self shielded" detector. The signal from the calorimeter is produced by the Čerenkov light generated in quartz fibers. The 200 keV Čerenkov threshold of quartz makes the detector insensitive to the Soft Bend synchrotron radiation, and reduces the effective size of the electromagnetic showers in the calorimeter (low energy tails produce no Čerenkov light). Placing the fibers perpendicular to the detector axis allows for a fine transverse segmentation, high linearity and uniformity of the response. Alternating the layers with vertical and horizontal fibers allows for a high position resolution in both directions.

Tests at the HFIR reactor showed [43] that the light attenuation in quartz fibers at 400 nm increased by approximately 10 dB/m after irradiation to 8 GRad by 1 MeV photons at 150°C, which would have a negligible effect on the QFC polarimeter performance. The actual dose accumulated during the SLD operation was estimated to be about 2 GRad. No signs of radiation damage had been observed.

4.1.2 Calorimeter design

The calorimeter is formed by a longitudinal stack of thirty four 3.5 mm thick (approximately one radiation length) tungsten plates (figure 4.1), which have precisely machined 14 mm wide grooves in alternatingly horizontal and vertical directions. The plates are shaped so that the device can be positioned very close to the electron beam pipe, and have a cut out to avoid scattering the synchrotron radiation stripe produced by the Hard Bend magnet. Thirty eight quartz fibers fit tightly inside each groove. Figure 4.2 shows a picture of several plates with fibers glued in. We used commercially available

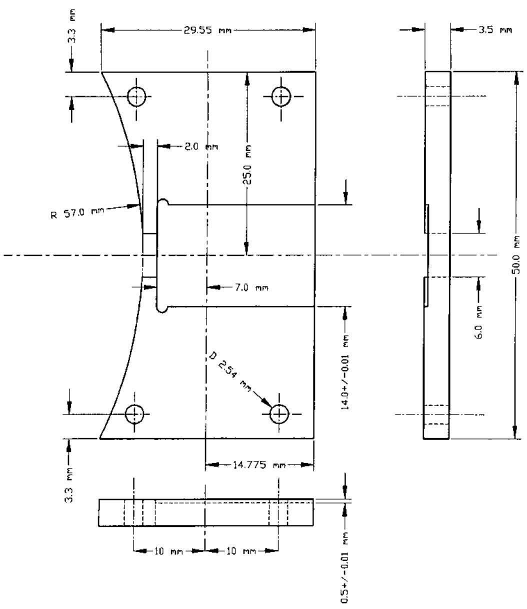

Figure 4.1: QFC design: tungsten plate with horizontal groove.

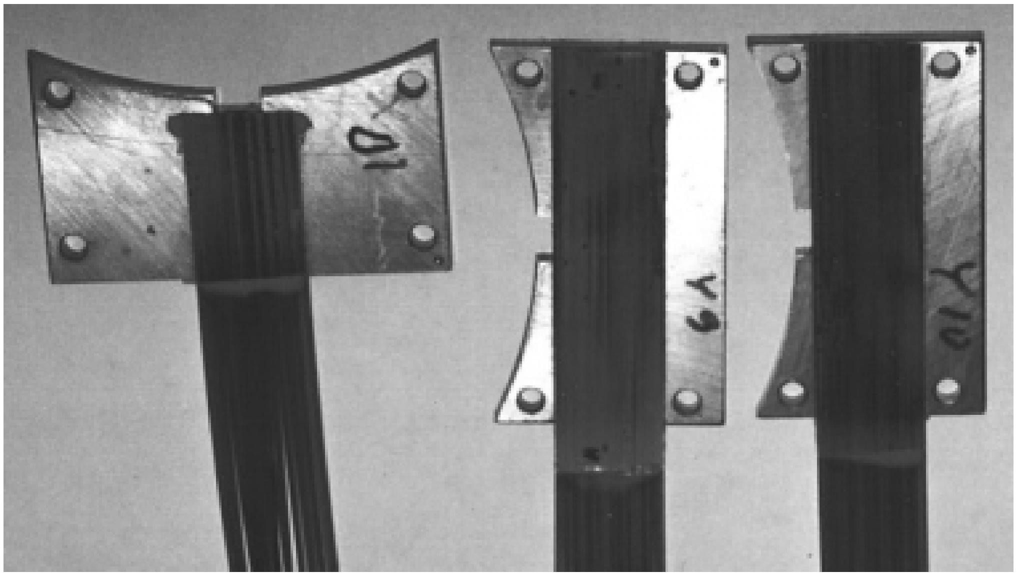

Figure 4.2: QFC design: tungsten plates with fibers glued in.

[44] polyimide buffered quartz fibers with $360\,\mu m$ outer diameter ($300\,\mu m$ pure silica core, $330\,\mu m$ outer diameter doped silica clad).

The grooves in the plates are aligned using two positioning pins. Two stainless steel tightening rods are used to keep the stack together (figure 4.3). The assembly is placed in a light-tight aluminum body (figure 4.4, 4.5).

The calorimeter was originally mounted on a remotely operated micrometer stage that allowed for position adjustment in both vertical and horizontal directions (figure 4.6). The stage had to be removed before the SLD 1997/98 run to make room for additional shielding.

The calorimeter segmentation scheme is shown in figure 4.7. Half of the fiber planes have transverse segmentation and are used for the position measurement. In each such plane, three adjacent fibers are grouped together, yielding a transverse segment size of approximately 1.1 mm. Fibers are also grouped longitudinally in vertical and horizontal layers thus forming two independent calorimeters for position measurements in two directions (vertical and horizontal). Layers with segmented readout are alternated with similar but unsegmented vertical and horizontal layers used for total energy measurement. Fibers from these layers are read out by two phototubes, one for vertical and one for horizontal fibers. One half of the fiber planes is therefore used for position measurements (10 coordinate channels in each direction) and the other half is used for total energy measurements (X-Amplitude and Y-Amplitude channels). The first and the last longitudinal layers have no transverse segmentation and are read out separately

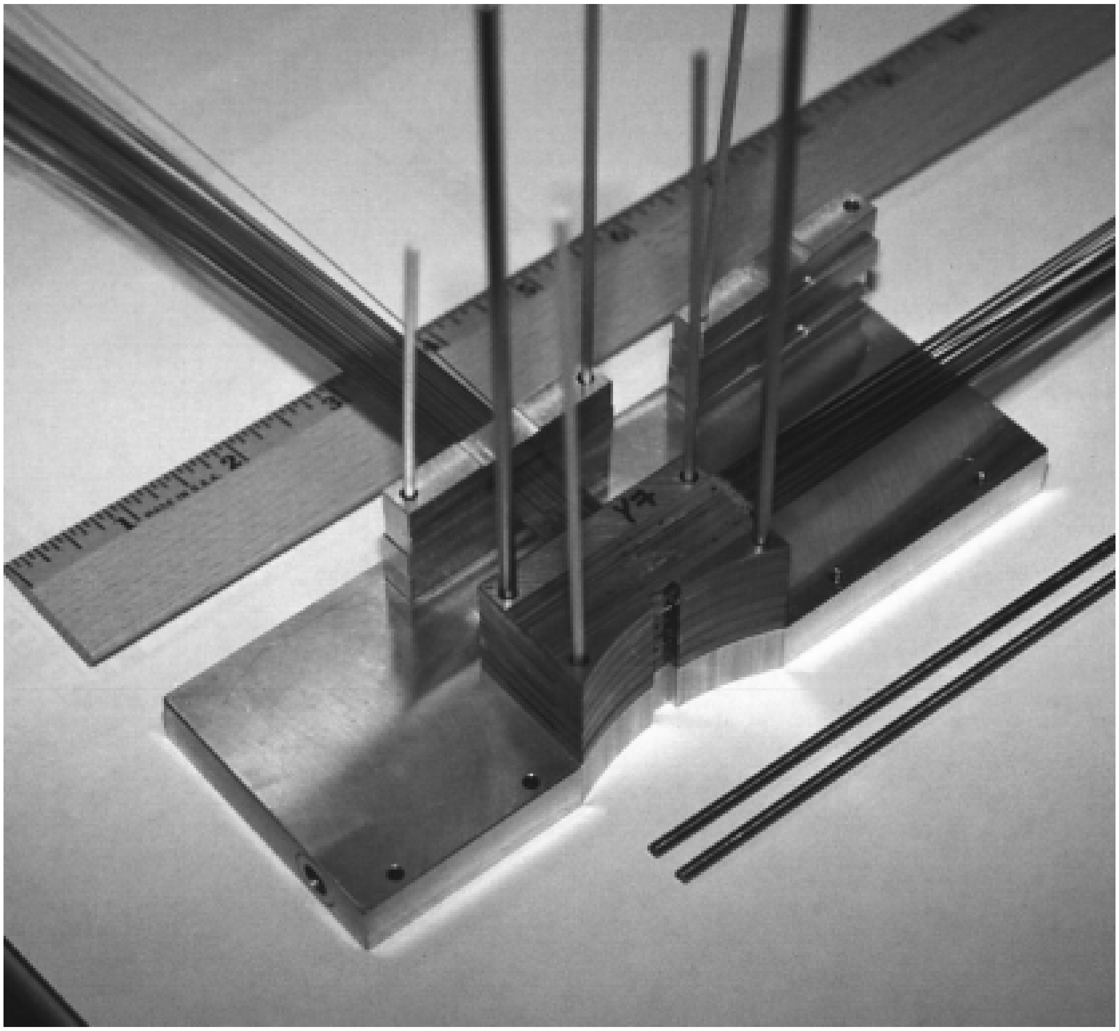

Figure 4.3: QFC design: positioning the absorber plates.

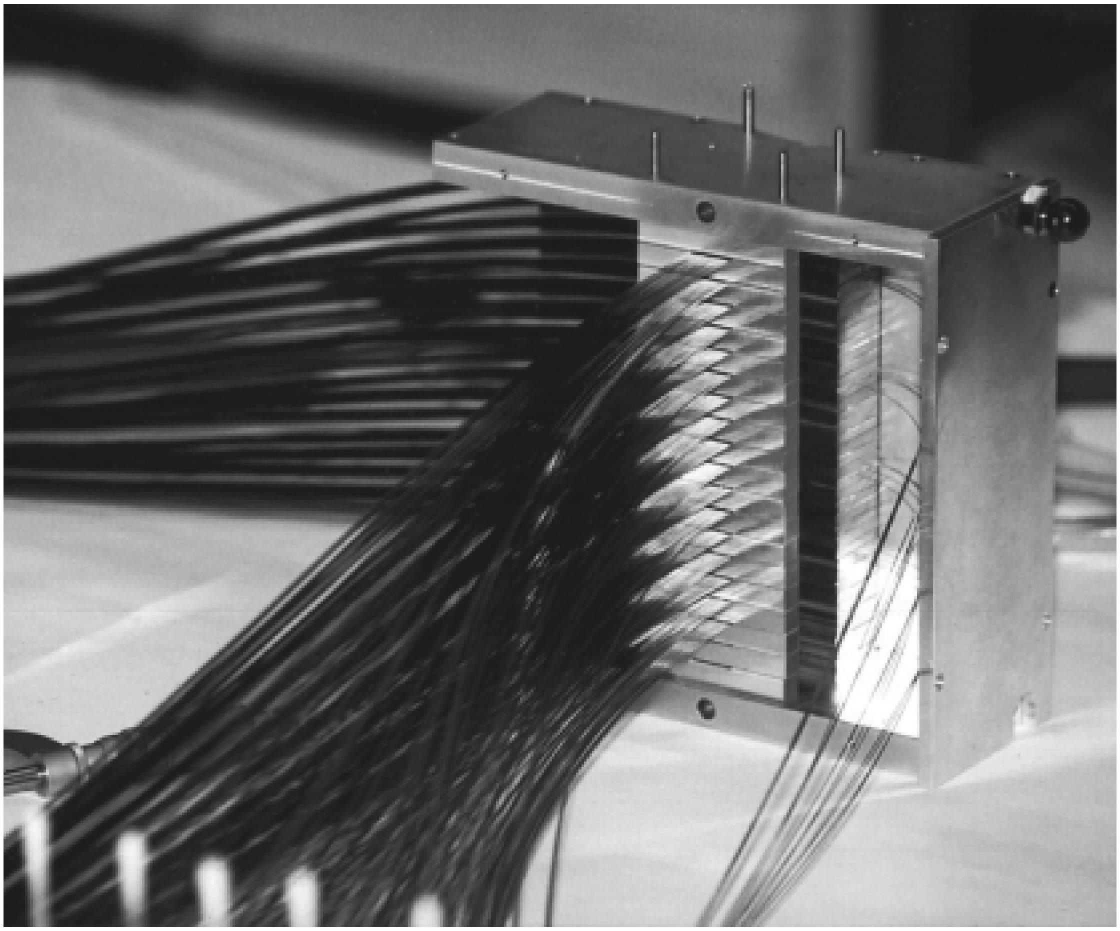

Figure 4.4: QFC design: calorimeter assembly.

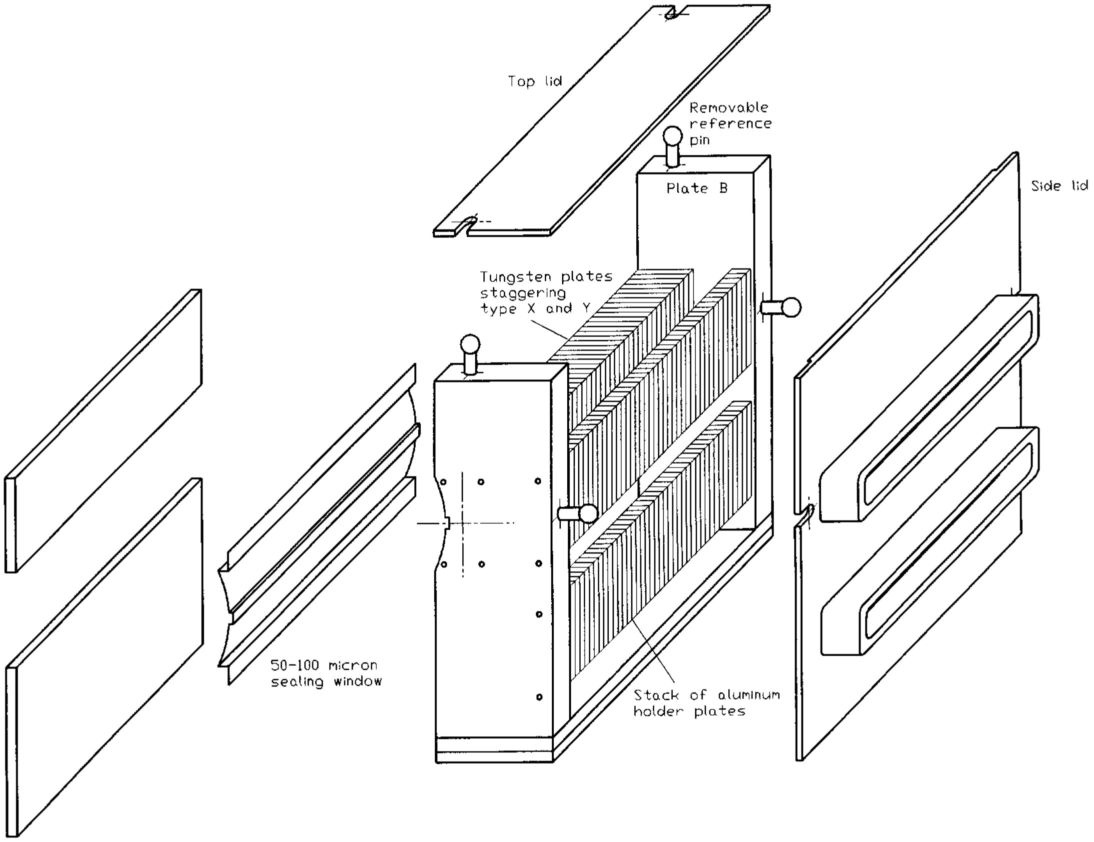

Figure 4.5: QFC design: light-tight aluminum body.

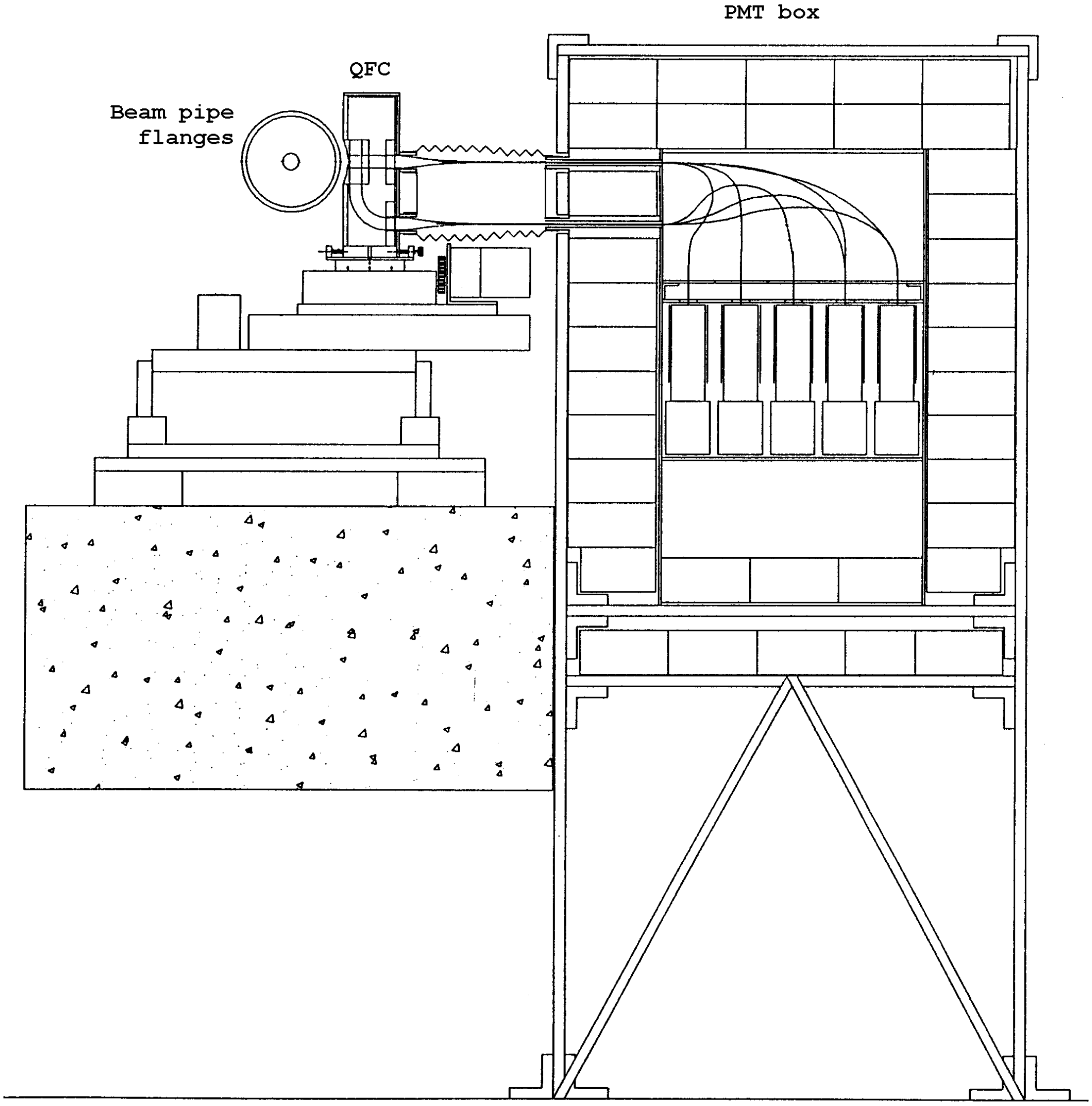

Figure 4.6: QFC polarimeter area layout.

to provide additional information on the background seen by the detector (Forward Background and Back Background channels).

4.1.3 Readout

Čerenkov light produced in the quartz fibers is read out by 24 phototubes placed in a lead-shielded box (figure 4.6). Air gaps between the ends of the fiber bundles and the PMT windows help to increase the uniformity of the detector response. After passing through phototube-mounted preampifiers, the signals are sent through 60 meter long coaxial shielded cables to the laser shack electronics room, where they are digitized by LeCroy 2249W ADCs and read out by the polarimeter data acquisition system (figure 4.8). Also shown in figure 4.8 is an LED calibration system used to monitor the channel gains and to study the readout linearity.

4.2 Polarimeter data selection

4.2.1 Procedure

The polarimeter acquires data at the SLC repetition rate of 120 Hz. The amount of data is very large - when all raw data is written to tape, the polarimeter accounts for approximately 20 % of all data logged by the SLD. In order to reduce the required tape space and facilitate the off-line analysis, the following procedure is adopted. The run is divided into $20,000$ events portions (each corresponding to approximately 3 minutes of uninterrupted running) called polruns. For each polrun, a summary data bank is

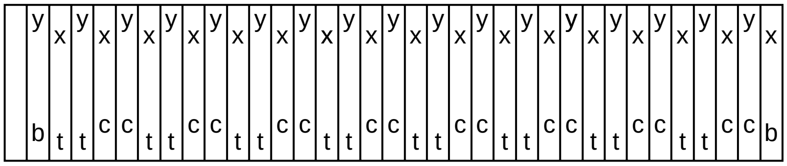

x - horizontal fibers
y - vertical fibers

t - layer for total energy measurement
c - layer for position measurement
b - layer read out separately

Figure 4.7: QFC segmentation scheme.

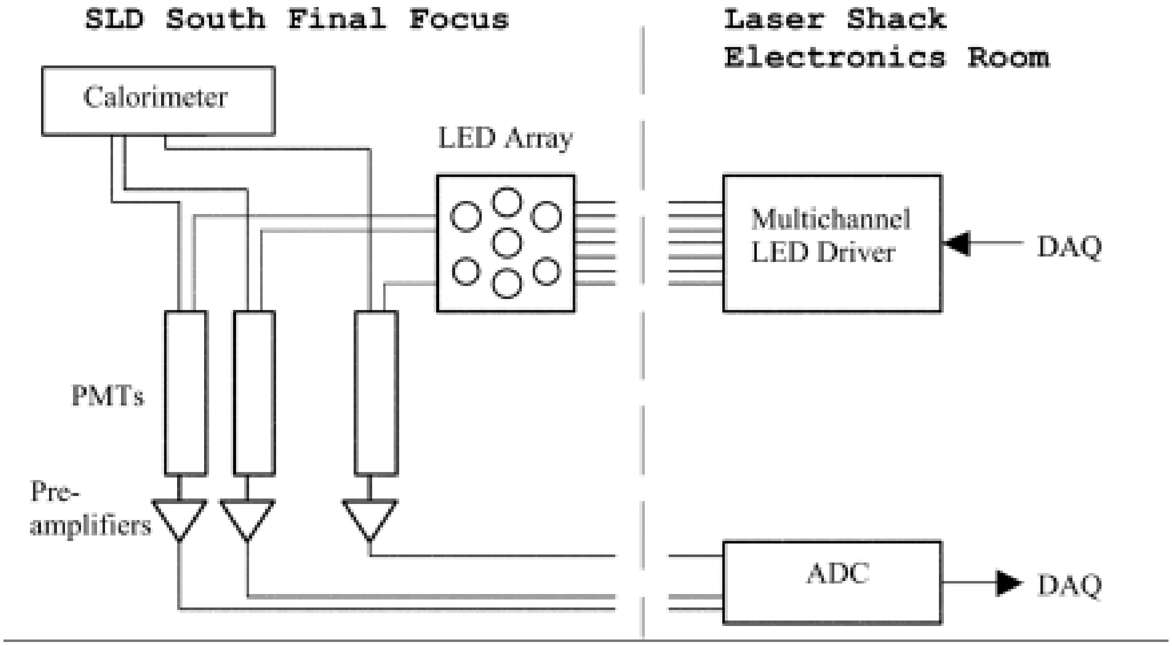

Figure 4.8: QFC readout scheme.

produced containing the number of events, channel sums, and channel squared sums for each of the polarimeter channels. Only events that pass online cuts are used to accumulate the sums, and the data is accumulated separately for each of the laser and electron beam helicity states, as well as for the laser off state. Along with the channel sums, the summary data banks contain other information describing the state of the machine and the detector during the polrun, such as the data acquisition system settings, type of calibration scan being performed, detector configuration, diagnostic parameters, etc. These data banks are written to tape and used in the mainstream polarimeter analysis.

Raw data is written to tape in separate data banks. During the normal running, only one of every 6 "laser off" events is written (which results in the equal numbers of "laser on" and "laser off" events being logged). The data volume is therefore reduced by a factor of 7/2. When necessary, the data acquisition system can be configured to write all events. Raw data can be used whenever summary data is insufficient for the analysis - for example, for various systematic errors studies.

4.2.2 Online cuts

Four cuts are applied to the data online on event by event basis. To ensure that electrons are present in the machine, cuts are made on the electron toroid (signal should be above 45 ADC counts) and the electron dumper (flag should not be set). To exclude noisy pulses, the signal in the CKV channel 9 is required to be below 1000 ADC counts (this channel is beyond the kinematic edge of scattered electrons, and therefore provides a convenient measure of the beam related noise). Finally, the electron beam polarization sign monitoring system is required to be in a consistent state as reported by the SLC.

4.2.3 Offline cuts

The cuts applied to the summary data off-line on polrun by polrun basis are listed in table 4.1. They are designed to ensure data quality in both the QFC and the CKV detectors, and to exclude the CKV calibration polruns.

4.2.4 Final data sample

Applying the cuts described above to the available electron-only data yielded a data sample equivalent to approximately 130 minutes of uninterrupted running, with most of the data (about 100 minutes) taken during the QFC dedicated study in December 1997. This data sample was used for the final comparison between the results of the polarization measurements by the QFC and the CKV detectors.

In addition, substantial amount of the QFC calibration and systematics study data was taken throughout the SLD 1997 run, usually in parallel to normal SLD running or various machine studies.

Table 4.1: QFC event selection off-line cuts.

Description	Value	Purpose
Number of events	> 400 in each of the four laser-on helicity states, $> 10,000$ background events.	Data quality.
Pockels Cell voltage	Nominal sequence, value within 50 V of nominal.	Exclude Pockels cell scans.
CKV PMT voltage	Within 2 V of nominal.	Exclude voltage scans.
CKV table position	Within 0.3 mm of nominal.	Exclude table scans.
CKV pre-radiator configuration	Nominal.	Data quality.
SLC reported status	Flag set by QBADPOL.	Data quality.
Compton laser status	Flag set by QLASDEF. Laser power setpoint is not below nominal.	Data quality. Exclude parts of laser power scans.
Electron toroid current	> 200 ADC counts.	Beam quality.
Positron toroid current	< 50 ADC counts.	Select electron only data.
CKV channel 7 average signal size	$30 < signal < 250$, ADC counts.	Signal in linear range.
QFC vertical amplitude channel average signal size	$50 < signal < 800$, ADC counts.	Signal in linear range, exclude noisy polruns.

4.3 Measuring experimental asymmetry

4.3.1 Determining the polarization by measuring the detector response asymmetry.

The first step in determining the polarization is to measure the asymmetry in the energy carried by the Compton photons, calculated for different electron-photon helicity combinations. We define the asymmetry A between two quantities X and Y as $A = (X - Y)/(X + Y)$, and will use the notation introduced in the section 3.4.1.

Because the QFC in a total absorption calorimeter, the signal it generates is proportional to the energy carried by the Compton photons that hit the detector. For each of the QFC channels, the response S is determined by

$$S \sim \int_{x,\phi} V(x,\phi) \left(\frac{d^2\sigma}{dx d\phi} \right)_{Comp} x\, dx\, d\phi \tag{4.1}$$

where $V(x,\phi)$ is the response function of this particular channel. Substituting the Compton cross section from 3.7, we get

$$S \sim \int V(x,\phi) \left(\frac{d^2\sigma}{dx d\phi} \right)_{unpol} \Big(1 - P_\gamma [P_e^z A_{e\gamma}^z(x) + P_e^t \cos\phi A_{e\gamma}^t(x)]\Big)\, x\, dx\, d\phi \tag{4.2}$$

The asymmetry between the signal produced by the detector when P_γ and P_e have opposite signs, and the signal produced when P_γ and P_e have the same sign, is given by

$$A \equiv \frac{S_- - S_+}{S_- + S_+} = |P_\gamma| \left(|P_e^z| a^z + |P_e^t| a^t\right) \tag{4.3}$$

where the analyzing powers a^z and a^t are

$$a^z = \frac{\int_{x,\phi} V(x,\phi) \left(\frac{d^2\sigma}{dx d\phi}\right)_{unpol} A^z_{e\gamma}(x)\, dx\, d\phi}{\int_{x,\phi} V(x,\phi) \left(\frac{d^2\sigma}{dx d\phi}\right)_{unpol} dx\, d\phi} \tag{4.4}$$

$$a^t = \frac{\int_{x,\phi} V(x,\phi) \left(\frac{d^2\sigma}{dx d\phi}\right)_{unpol} \cos\phi\, A^t_{e\gamma}(x)\, dx\, d\phi}{\int_{x,\phi} V(x,\phi) \left(\frac{d^2\sigma}{dx d\phi}\right)_{unpol} dx\, d\phi} \tag{4.5}$$

For the amplitude channels whose response is simply proportional to the total energy carried by the Compton photons (assuming a perfectly linear calorimeter that absorbs all photons produced in the scattering. We postpone the discussion of small corrections and systematic uncertainties associated with this assumption until section 4.4.2), the response function $V(x,\phi)$ is constant across the range of x and ϕ, and the integration over ϕ cancels out the term proportional to the transverse component of the electron polarization. Therefore, 4.4 can be rewritten for these channels as

$$a^z_{amp} = \frac{\int_{x=0}^{1} \left(\frac{d\sigma}{dx}\right)_{unpol} A^z_{e\gamma}(x)\, dx}{\int_{x=0}^{1} \left(\frac{d\sigma}{dx}\right)_{unpol} dx} = 0.17332 \tag{4.6}$$

and the longitudinal component of the electron polarization can be found as

$$P_e^z = \frac{A_{amp}}{P_\gamma \, a_{amp}^z} \tag{4.7}$$

where A_{amp} is the asymmetry measured by the amplitude channels :

$$A_{amp} = \frac{S_{J=3/2} - S_{J=1/2}}{S_{J=3/2} + S_{J=1/2}} \tag{4.8}$$

The notation $S_{J=3/2}$ and $S_{J=1/2}$ emphasizes the fact that, according to the sign convention we adopted (see section 3.4.1), P_e and P_γ have opposite signs when the electron and the photon helicities are parallel, and the same sign when they are anti-parallel.

For coordinate channels, the response functions can be determined using Monte Carlo simulation. Expression 4.3 can then be reversed to calculate the transverse polarization starting from the measured asymmetry. In our case, no independent information on the beam size was available, and the analyzing powers produced by the simulation had to be parameterized by the beam shape parameters. We used the amplitude channels to determine the longitudinal polarization, and then extracted the transverse polarization and the beam size parameters simultaneously by fitting the asymmetries observed in all available coordinate channels to the function defined by equation 4.3. Note that this method does not require any knowledge of the relative gains of the QFC channels.

4.3.2 Asymmetry calculation

Because the signs of both the laser and the electron beam polarizations are flipped randomly on event-by-event basis, and the laser only fires on every seventh machine pulse, we have six types of signals coming from the detector : S_{RR}, S_{RL}, S_{LR}, S_{LL}, S_{RO}, and S_{LO}, where the first subscript corresponds to the electron helicity (right or left), and the second subscript corresponds to the photon helicity(right, left, or laser off). The laser off events provide a measure of the background seen by the detector. Figure 4.9 shows typical signal distributions for one of the QFC channels. The experimental asymmetry is formed as

$$A = \frac{S_{RL} + S_{LR} - S_{RR} - S_{LL}}{S_{RL} + S_{LR} + S_{RR} + S_{LL} - 2(S_{RO} + S_{LO})} \tag{4.9}$$

Note that the asymmetry calculated in this way is a fairly robust quantity. While currents and polarizations of both the laser and the electron beams can have slight (less than 10^{-3}) left-right asymmetries, they automatically cancel out in the first order from the expression 4.8.

4.3.3 Statistical errors

This section discusses the statistical errors of the asymmetry measurement, which determine the time needed to achieve the desired accuracy. This in an important issue for the QFC polarimeter because the measurement cannot be performed in parallel to taking physics data with the SLD detector (to avoid huge background caused by beamstrahlung), and dedicated time has to be allocated for it. When the detector was

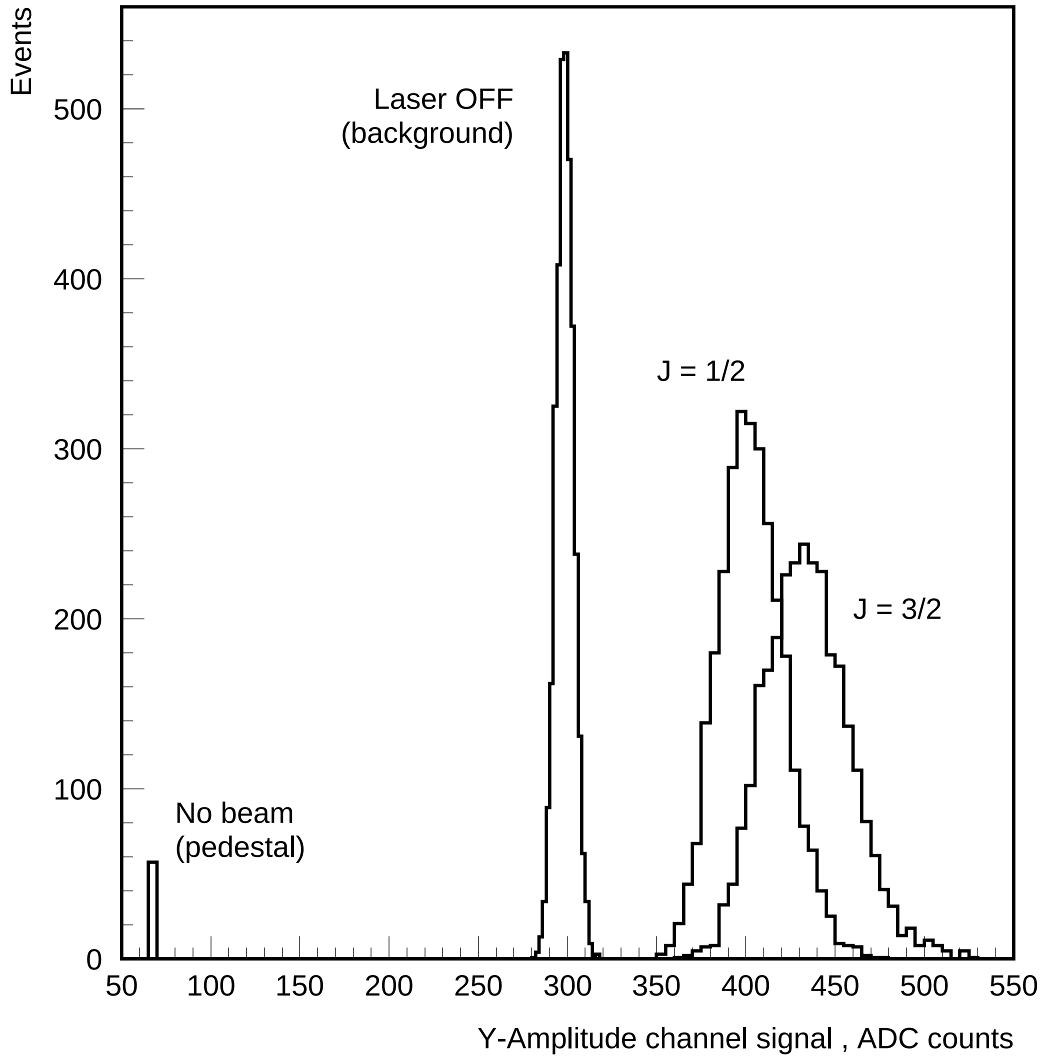

Figure 4.9: QFC signal distributions.

first installed and tested, backgrounds in the amplitude channels exceeded the signal by more than two orders of magnitude, and the resulted statistical errors made a precise polarization measurement impossible. We used the SLD 1996 run to carry out a number of studies to identify the sources of the background and find a way to reduce it to acceptable levels. As a result, an average statistical error in the measured polarization was reduced to about 2.5 % per 3 minute polarimeter run (about 20000 machine pulses), and was dominated by fluctuations in the effective luminosity of the electron and the photon beam collisions. This allowed to achieve our target accuracy of 0.5 % in less than 3 hours of data taking. The rest of this section describes the three major sources of statistical errors : background, pulse to pulse fluctuations in the number of Compton photons, and the QFC energy resolution.

Background

The overwhelming level of background observed during our first attempts to measure the beam polarization with the QFC forced us to undertake a detailed study of the background [45]. Two major sources of the background were identified: scattered synchrotron radiation from the hard bend magnet, and a low energy halo around the beam produced by the beam tails in the upstream collimators and quadrupoles.

After passing the Compton interaction point, the electron beam is bent horizontally by a pair of dipole magnets (figure 4.10), generating a high flux of synchrotron radiation. The first of the two magnets, the Soft Bend magnet, has a magnetic field of 0.385 kGauss and produces a deflection angle of 1.0 mrad, generating 462 TeV of synchrotron radiation

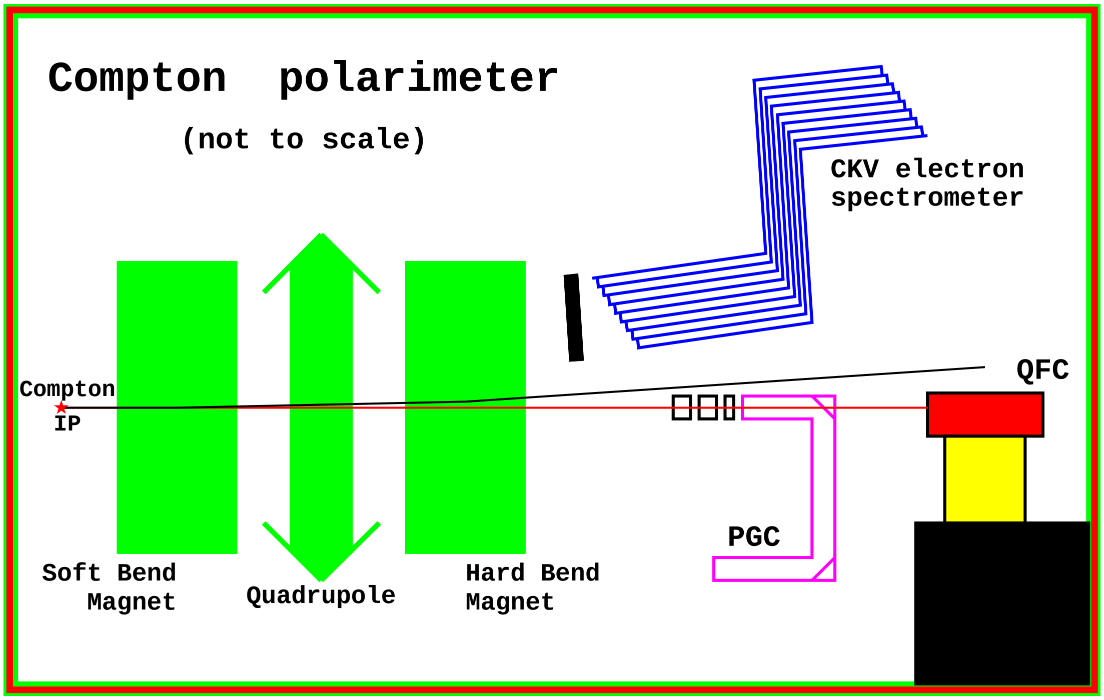

Figure 4.10: Compton polarimeter layout.

per electron bunch (as compared to about 15 TeV energy carried by Compton photons) with a critical energy of 53.2 keV. This radiation, as well as synchrotron radiation generated by the core of the electron beam in upstream quadrupoles, is effectively suppressed by the Čerenkov threshold of the quartz fibers (198 keV for electrons). The second dipole magnet, the Hard Bend magnet, has a field value of 11.69 kGauss and a bending angle of 17.3 mrad, producing $2.43 \cdot 10^5$ TeV of synchrotron radiation with a critical energy of 1.62 MeV. Due to the deflection of the electron beam by the Soft Bend magnet prior to the entry into the Hard Bend, there is 1 mrad separation between the direction of the neutral beam (Compton photons) and the beginning of the Hard Bend synchrotron stripe, which gives a 9 mm displacement at the location of the QFC detector.

Our original intention was to design and position the detector in a way that would ensure no scattering of the Hard Bend synchrotron stripe in the vicinity of the calorimeter. The absorber plates were shaped to let the Hard Bend synchrotron photons through without interaction. However, while this solution can be definitely used for the future e^+e^- colliders, it proved to be very difficult to implement for the SLD experiment, where the beam layout in the polarimeter area was not designed with a Compton photon detector in mind. Due to very limited space available for the QFC, it had to be placed near beam pipe flanges and a collimator, which scatter synchrotron radiation onto the detector. Our studies showed that this radiation was the major source of the background seen by the QFC. It was very stable, scaled with the electron beam current, and did not depend on other beam parameters.

The background produced by the Hard Bend synchrotron radiation was simulated [45] using the GEANT package. Details of the simulation can be found in appendix B. Comparison of the ratios of background signals in various types of the QFC channels between data and Monte Carlo confirmed that our simulation was fairly accurate. We then used it to optimize the shielding configuration around the detector. While the most efficient shielding concept would be to intercept the synchrotron stripe as far upstream from the QFC detector as possible, we were limited by the need to avoid creating additional backgrounds and possibly asymmetry contamination [46] for other detectors located in the area - most noticeably for the CKV detector. After extensive Monte Carlo study, we settled on a compromise configuration which allowed for achieving about 1:2 signal-to-background ratio in the amplitude channels - as compared to about 1:115 ratio observed during the SLD 1996 run.

The other source of the background was the low energy halo around the beam produced by the beam tails in the upstream collimators and quadrupoles. While being much smaller in magnitude than the background due to the scattered Hard Bend synchrotron radiation, this component was highly variable and contributed significantly to the statistical error of the polarization measurement. Since it was very sensitive to the beam steering, we were able to tune the beam to minimize the halo. Combined with tight shielding of all sides of the detector, especially of the transport fibers going from the calorimeter to the PMT box, beam tuning resulted in almost complete elimination of this background component.

QFC energy resolution

The energy resolution of the QFC is determined by the shower fluctuations and the photoelectron statistics. Since the average total energy carried by the Compton photons in a single machine pulse is about 15 TeV, the requirements for calorimeter energy resolution are fairly relaxed. Based on the beam test results which are in excellent agreement with Monte Carlo predictions, the resolution for 15 TeV of the incident energy (in the form of Compton photons in the 0 to 28.25 GeV energy range) is estimated to be 1.9 % for each of the amplitude channels.

Fluctuations in the energy carried by the Compton photons

The average total energy of the Compton photons generated per machine pulse is about 15 TeV. Taking into account the shape of the energy spectrum, this corresponds to approximately 3.6 % fluctuations in the total energy.

However, the dominating source of statistical error is an uncertainty in the luminosity of the electron and the photon beams collisions caused by pulse to pulse fluctuations in the beams intensities, timing and position jitter. The size of this effect depends on the running conditions. For the data sample that was used for the QFC versus CKV comparison, the resulting fluctuations in the Compton signal amplitude were about 17 % (RMS) on the average.

4.4 Longitudinal polarization measurement

4.4.1 Analyzing power

As shown in section 4.3.1, the longitudinal polarization of the electron beam can be determined from the experimental asymmetries measured by the QFC amplitude channels using the equation 4.6, with the analyzing power being equal, in the first approximation, the the asymmetry in the total energy carried by the scattered photons : $a^z_{amp} = 0.17332$. In order to account for the limited angular acceptance of the detector, finite beam size, and possible nonlinearity of the energy response function, the analyzing powers used in the analysis were deduced from the detailed Monte Carlo simulation of the calorimeter and surrounding beam line elements (see appendix B for details). The simulation yielded the following analyzing powers for the two QFC amplitude channels:

$$a^z_X = 0.17338$$

$$a^z_Y = 0.17366$$

where the subscripts X and Y mark the channels containing horizontal and vertical fibers respectively.

4.4.2 Systematic uncertainties

The summary of the QFC systematic errors relevant to the longitudinal polarization measurement using amplitude channels is given in table 4.2 Details on various sources of systematics are given in the rest of this section.

Table 4.2: QFC: summary of systematic errors of the longitudinal polarization measurement. Numbers are given in per cent.

Calorimeter		
Angular acceptance, finite beam size	small	Compton cross section angular dependence, Monte Carlo simulation.
Energy response function linearity	0.2	Monte Carlo simulation, beam test.
Detector misalignment	0.1	Monte Carlo simulation, beam test.
Local non-uniformity	0.3	Monte Carlo simulation, beam test.
Optical cross talk	small	Measurement, Monte Carlo simulation.
Asymmetry contamination by re-scattered electrons	small	Monte Carlo simulation, *in situ* study.
Readout		
Readout linearity	0.5	LED study, beam test.
Electronic cross talk	0.1	*In situ* study.
Laser pickup	0.1	Direct measurement.
Total	0.6	

Angular acceptance and the beam size

Since the angular divergence of the photon beam due to the Compton scattering is extremely small, the correction to the analyzing power caused by the limited angular acceptance of the detector is negligible (of the order of 10^{-5} for a point-like incident electron beam). Due to the real shape of the electron beam, the Compton spot size at the entry to the QFC is approximately 400 x 91 microns. This realistic beam size, together with the actual Compton photons angular distribution, was used in the Monte Carlo simulation. However, since the real beam parameters are not precisely known, we need to estimate the effect of an error in the beam size on the error in the QFC analyzing power. In order to do this, three beam configurations were simulated: point-like beam, realistic beam, and a round beam 800 x 800 microns (double size in horizontal direction). All three simulations yielded identical analyzing powers within 0.05 % - a negligible effect compared to other sources of systematic uncertainties. The study assumed perfect alignment between the calorimeter and the beam. Possible effects of the position and angular misalignment will be discussed later.

Energy response function

The relative difference between the theoretical analyzing power obtained by integration over the Compton spectrum, and the analyzing power determined by the Monte Carlo simulation, is 0.03 % and 0.19 % for the X-amplitude and Y-amplitude channels respectively. Since the effects of angular acceptance and finite beam size were found to be negligible, this difference is due entirely to the nonlinearity of the simulated energy response function (the dependence between the photon energy and the calorimeter response) of the detector, which could be caused by shower leakage, Čerenkov threshold of the quartz fibers, and other effects. The energy response function was measured in the beam test in the 5-25 GeV range and found to be consistent with the Monte Carlo predictions (figure 4.11).

However, since, due to the test beam facility limitations, we were unable to precisely measure the response function in the whole range of possible Compton photon energies (from 0 to 28.25 GeV), we conservatively include the maximum difference of 0.2 % between the analyzing power obtained with the Monte Carlo simulation, and the analyzing power calculated under assumption of perfect linearity of the detector response function, in our estimate for the systematic error of the polarization measurement.

Since the beam test was performed after the polarization measurements, the measured energy response function also included any effects of the possible radiation damage to the quartz fibers (even though we did not see any evidence of such damage).

Calorimeter misalignment

Survey data and the calorimeter's own position sensitivity allow for reliable determination of its position and angle with respect to the Compton beam with an accuracy of ±100 microns and ±0.7 degrees respectively (both are very conservative estimates, careful analysis of the information from the QFC coordinate channels allows for much better accuracy. However, there is no need to do such analysis for all the data). Within

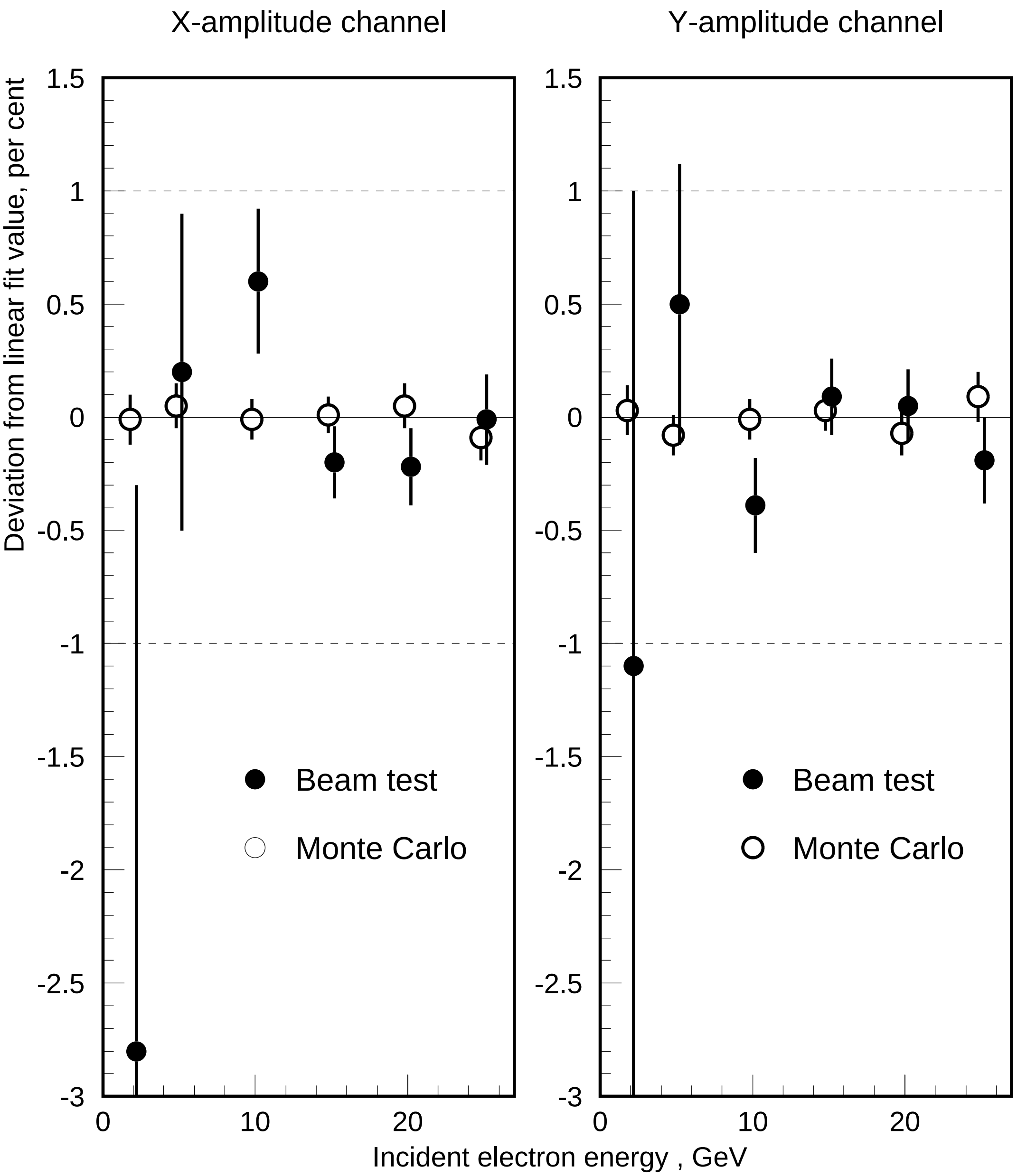

Figure 4.11: QFC energy response function: residuals to the linear fit.

these limits, the effects of angular and position misalignment of the calorimeter with respect to the nominal beam line were studied both in Monte Carlo simulation and in the beam test. While we saw a sizeable effect of the angular misalignment on the asymmetry in coordinate channels, the asymmetry measured by the amplitude channels used for the longitudinal polarization measurement was unaffected at 0.1 % level.

Local non-uniformity in the calorimeter

We use the term "local non-uniformity" to describe deviations of the QFC real geometry from the nominal design due to mechanical tolerances associated with the calorimeter construction process. The nominal geometry was assumed in the Monte Carlo simulation that was used to calculate the analyzing powers. We identified several categories of deviations from the nominal geometry that could in principle affect the measured asymmetry:

- fluctuations in the thicknesses of the absorber plates;
- misalignments between grooves in different absorber plates;
- uncertainty in the position of fibers inside the absorber groove (since the groove is slightly wider than the sum of outer diameters of all fibers inside it);
- fiber to fiber variations in the light attenuation length;
- uncertainty in the fibers path between the calorimeter and the phototube box.

All these categories were studied in Monte Carlo using the actual Compton beam parameters, and all except one were found to have negligible effects on the asymmetry in the amplitude channels. For these channels, the biggest potential problem is represented by the uncertainty in the fibers path between the calorimeter proper and the PMT box.

Since the fibers configuration in this "transport" region was only roughly known (fibers were attached to the calorimeter on one end, and to the phototubes on the other, but could follow any path in the middle, restricted only by the walls of the channel in shielding), we used the following method to obtain an estimate for a systematic error associated with this uncertainty. The analyzing powers used in the analysis were generated using “nominal” fiber configuration in the transport region that represented our best educated guess. This nominal configuration was used for all other Monte Carlo studies. Six other configurations representing qualitatively different possible fibers paths in this region were also simulated. For each configuration, the signal generated in the fibers in the transport region and its asymmetry were estimated separately from the signal (and associated asymmetry) generated in the calorimeter proper. The results are listed in table 4.3. For the nominal geometry, the effect of the transport region signal on the total measured asymmetry was found to be very small (less than 10^{-4}). For all configurations, the portion of the signal generated in the transport region was in the range from 0.03 to 0.56 % of the total signal, while the relative difference between its asymmetry and the asymmetry in the total signal changed between -48.3 and +9.9 % of the total asymmetry. Combining the highest signal in the transport region with

Table 4.3: QFC: signal and asymmetry in the transport region between the calorimeter and the PMT box. The signal picked up by the fibers in the transport region is given in per cent of the total signal in the corresponding channel, for parallel helicities of the incident electrons and photons. Asymmetry deviation is the difference between the asymmetry of the transport region signal and the asymmetry of the total signal, in per cent of the total signal asymmetry. 100 % longitudinal polarization of the incident electron beam is assumed in the simulation.

Fiber path	X-amplitude channel			Y-amplitude channel		
	Signal	Asymmetry deviation	Effect on total asymmetry	Signal	Asymmetry deviation	Effect on total asymmetry
Nominal	0.26 %	+ 2.1 %	+ 0.01 %	0.19 %	+ 1.0 %	0.00 %
A	0.41 %	- 29.2 %	- 0.12 %	0.18 %	- 16.3 %	- 0.03 %
B	0.30 %	+ 8.1 %	+ 0.02	0.24 %	+ 0.9 %	0.00 %
C	0.11 %	- 48.3 %	- 0.06 %	0.03 %	- 39.6 %	- 0.01 %
D	0.56 %	+ 9.9 %	+ 0.05 %	0.39 %	+ 8.5 %	+ 0.03 %
E	0.23 %	-22.2 %	- 0.05 %	0.27 %	- 27.9 %	- 0.08 %

the highest asymmetry deviation, we obtain a conservative estimate of 0.3 % for the associated systematic error.

Optical cross talk

Since the fibers in each of the QFC longitudinal layers lie close to each other in the tungsten plate grooves, and all fibers follow the same path from the calorimeter to the phototube box, there is a chance that Čerenkov photons generated in one fiber can escape it and be captured by another fiber that belongs to a different channel, thus creating a cross talk. Our choice of clad fibers should make this effect very small. Simple test was done in order to verify this - a number of fibers were bundled together, and light from an LED source was sent through some of them. The fibers not connected to the light source were read out by a phototube, and the difference between the "LED ON" and "LED OFF" signals was measured. No cross talk was detected at 10^{-3} level, which implies completely negligible effect on the measured asymmetry since asymmetries in most fibers are close to each other.

Asymmetry contamination by re-scattered Compton electrons

Compton scattered electrons are analyzed by the CKV detector located on the opposite side of the beam pipe from the QFC. Electrons of different energies have different asymmetries ranging approximately from -0.26 to 0.75, and after going through a pair of dipole magnets, they are separated in space. Therefore, care should be taken to avoid re-scattering Compton electrons onto the QFC detector where they could contaminate the measured asymmetry. The problem was studied in Monte Carlo simulation, and no effect on the asymmetry was observed at 10^{-4} level. To confirm this conclusion experimentally, a portion of the data was taken with the CKV detector moved away from the beam.

Readout linearity

The linearity of the QFC readout was studied using the LED calibration system by measuring the dependence between the strength of the LED pulse and the ADC output. It was also checked in the beam test by looking at the dependence between the electron beam intensity (at a fixed energy) and the output signal. Both methods probe the response function of the complete readout chain including the phototube, the preamplifier, 60 meters long coaxial cable, and the ADC (figure 4.8). Both have their limitations however: LED pulse shape is different from the pulse shape of the actual Compton signal, and the beam test data could be affected by nonlinearities in the response of the Čerenkov counter that was used to control the beam intensity (the counter was precisely calibrated by the E144 experiment [47] so the effect should be small). For these reasons, we do not apply corrections associated with the measured electronics response function to the data, but rather include the effect of the observed deviation from linearity in our estimate for the systematic error. Consistency of the results obtained by two independent methods gives us confidence in the correctness of our estimate.

The QFC LED calibration system includes 7 LEDs. Any subset of these can be fired on any given data acquisition cycle. The light produced by the LEDs is picked up by 30 quartz fibers, each of which can be connected to a different QFC readout phototube. When all 7 LEDs are fired simultaneously, all fibers pick up approximately equal amount of light (within 5 %). However, when only one of the side-mounted LEDs is fired, the amount of light in different fibers can differ by order of magnitude. This feature was utilized for the QFC readout linearity study. Several methods were used (determination of differential response function by measuring the response to a small light pulse on top of another light pulse of variable size, measuring the ratio of signals produced by light pulses of different strengths while varying the high voltage settings, etc.) and produced consistent results. The most direct (and most precise) method is described below.

In this method, we chose an LED that produced signal in the channel being tested that was several times bigger than the signals produced in a few other channels ("control channels"), so that the whole dynamic range of the tested channel could be spanned while keeping the signal low in control channels. We then varied the LED pulse strength, and measured the signal in the tested channel as a function of the amount of light produced by the LED, as measured by control channels. Consistent results obtained with different sets of control channels and different LEDs confirmed that the measured response function was not significantly affected by nonlinearities in the control channels themselves. PMT gains were monitored throughout this study by simultaneously taking data with the center mounted LED that was sending approximately the same amount of light into each channel. The pulse strength of this LED remained unchanged, so it could be used to check the relative gains of the tested channel and the control channels. Figure 4.12 shows an example of the measured response function for the X-amplitude channel. Residuals to the straight line fit are shown in figure 4.13. In order to calculate the effect on the measured asymmetry, the response function needs to be convoluted with the QFC signal distributions. For the data sample used for the QFC versus CKV comparison, the effect on the experimental asymmetry was found to be 0.1 ± 0.5 % for the X-amplitude, and 0.0 ± 0.4 % for the Y-amplitude channels.

In the beam test, we measured the QFC response as a function of the electron beam intensity, monitored by a calibrated Čerenkov counter. The measured dependence for the X-amplitude channel is shown in figure 4.14, and the residuals to the straight line fit are shown in figure 4.15. The corresponding effects on the measured Compton signal asymmetry are 0.3 ± 0.5 % for the X-amplitude, and -0.1 ± 0.5 % for the Y-amplitude channels.

Based on these results, we set a limit of 0.5 % on the contribution to the QFC systematic error from the readout nonlinearity, further confirmed by the high voltage scan and laser power scan cross checks described later in this section.

Electronic cross talk

We used the Compton signal itself to study the effects of the electronic cross talk in order to ensure that the system was tested under exactly the same conditions as experienced during the actual polarization measurement. The effect was studied in two ways. First, we switched high voltage off for one of the QFC channels during normal data taking to

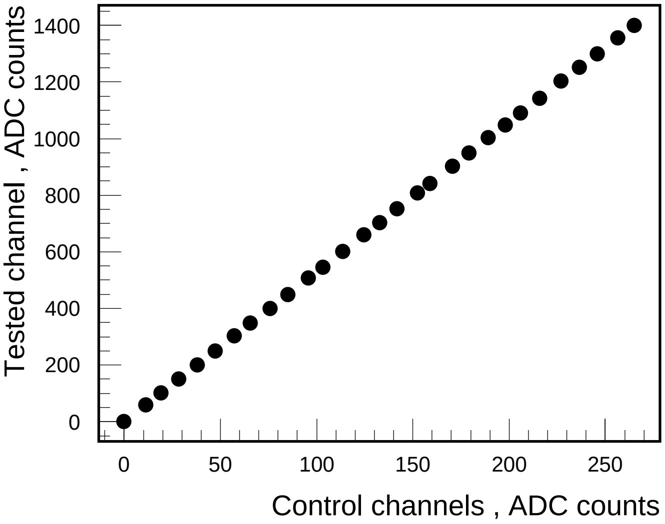

Figure 4.12: QFC readout linearity, LED test: X-amplitude channel response function. Signal in the tested channel as a function of the weighted average of the signals in control channels, pedestals are subtracted.

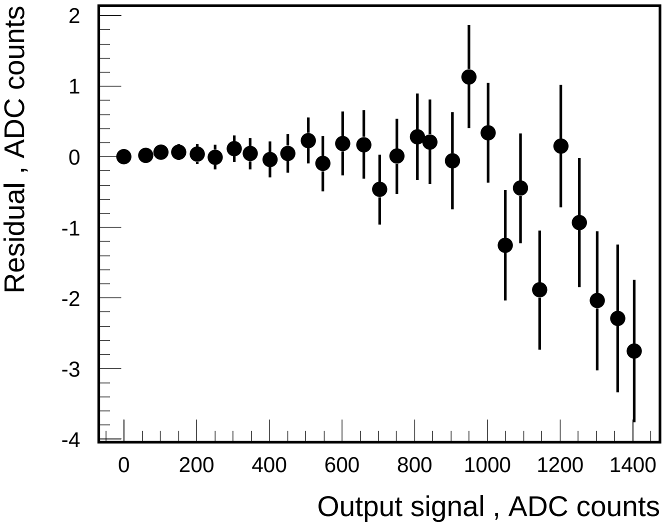

Figure 4.13: QFC readout linearity, LED test: X-amplitude channel response function, residuals to the linear fit.

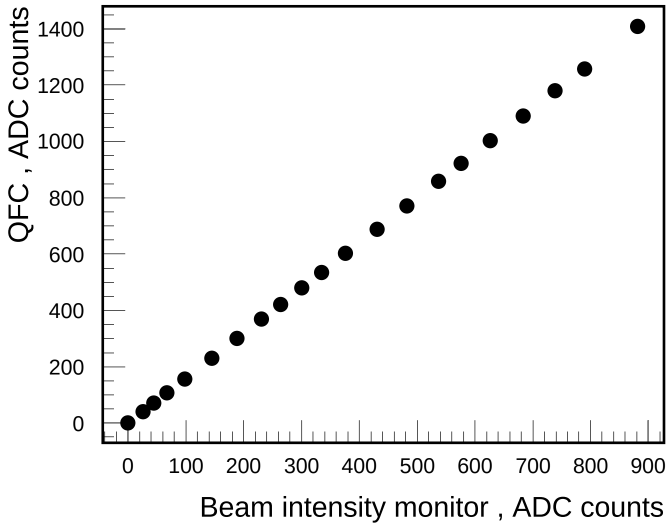

Figure 4.14: QFC readout linearity, beam test: X-amplitude channel response function. Signal in the tested channel as a function of the beam intensity measured by a calibrated Čerenkov counter, pedestals are subtracted.

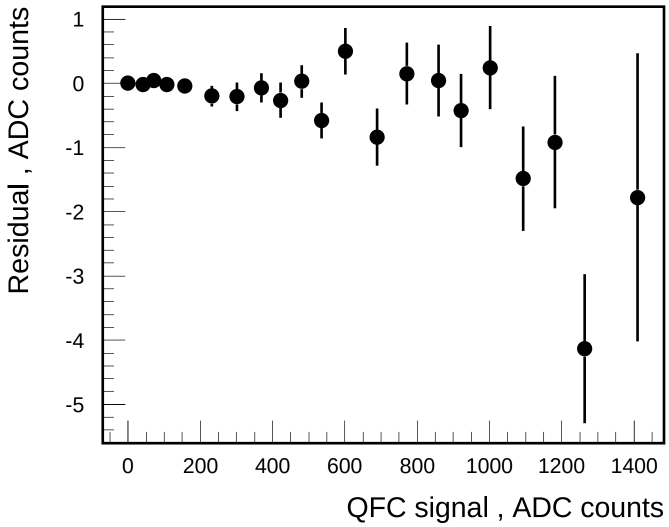

Figure 4.15: QFC readout linearity, beam test: X-amplitude channel response function, residuals to the linear fit.

see if there was any cross talk from the remaining 24 channels. Then, we switched off all channels but one to see if that channel created any cross talk in the other channels. The study was repeated for all QFC channels. Both methods showed no effect at the 0.1 ADC counts level - which corresponds to less than 0.1 % effect on the measured asymmetry in the amplitude channels.

Laser pickup

The QFC readout electronics is located in the outer room of the Compton laser shack. Since the electronics is not perfectly isolated from the laser room, very fast high voltage pulses of the laser Q-switch can generate small signals in the polarimeter readout channels. This effect is known as a "laser pickup" and requires small corrections to be applied to the asymmetry measured by the polarimeter.

In the normal course of the SLC running, there are always machine pulses with no electron beam present in the Final Focus. Such pulses are identified by the requirement that the electron toroids signals should be less than 35 ADC counts above pedestal (normal beam-on signals are about 400 ADC counts) and the signals in all CKV channels should be less than 70 ADC counts above pedestal. The difference between "LASER ON" and "LASER OFF" signals for no-beam pulses provides a measure of the laser pickup.

We found that for the QFC detector, the laser pickup was in the range from 0 to -0.1 ADC counts for most channels, including amplitude channels, under normal running conditions. For a typical Compton signal in these channels (about 120 ADC counts, background subtracted), the effect on the measured asymmetry was a little less than 0.1 %.

For the data sample used for the QFC versus CKV comparison, the measured laser pickup is -0.05 ADC counts for the horizontal amplitude channel, and -0.06 ADC counts for the vertical amplitude channel. The corresponding corrections of -0.03 % and -0.05 % respectively are applied to the measured asymmetries. Since the machine pulses used to estimate the laser pickup are not the same pulses used for the polarization measurement, we conservatively associate an additional 0.1 % systematic error with this effect.

4.4.3 Cross checks

Throughout the SLD 1997 run, we performed several cross check studies in order to verify the correctness of our understanding of the QFC detector and its systematic errors. These studies are described here.

High voltage scan

To check the linearity on the detector readout, we took data using different sets of the PMT high voltages. During the QFC systematics study in July 1997, we ran half of the time with nominal voltages on all channels, then reduced the voltages by approximately 100 V in half of the channels, including one of the amplitude channels, which caused the signals in these channels to drop by a factor of $2 \div 3$. The results of the measurements with both high voltage sets are presented in table 4.4 for the amplitude channels. The difference between the polarization values measured by the two amplitude channels

Table 4.4: QFC systematics cross check: high voltage scan.

	Nominal HV	HV reduced in Y-Amplitude channel
Average ratio of signal sizes in X-amplitude and Y-amplitude channels	0.98	2.22
Average polarization measured by X-amplitude channel	0.7182 ± 0.0024	0.7179 ± 0.0028
Average polarization measured by Y-amplitude channel	0.7203 ± 0.0024	0.7211 ± 0.0027
Relative difference in measured polarization, per cent	-0.29	-0.44

changed by less than 0.2 %, even though the signal size in one of them decreased by more than factor of 2. Other channels showed similar behavior.

Laser power scan

Another cross check of the detector linearity was performed by varying the laser power settings while taking data during the QFC systematics study in July 1997. The results were consistent with linear behavior, but the precision was limited by low statistics. Our original intention was to compare the results obtained with different laser powers to the polarization measured at the same time by the CKV detector, but this could not be done because the CKV experienced instrumental problems at the time of this study, and could not provide sufficient accuracy.

Beam optics configuration effects

The bulk of the QFC data used for the QFC versus CKV comparison was taken in the “narrow beam” mode - currents in two of the North Final Focus quadrupoles were scaled down to provide for a narrower beam through the Final Focus and reduce the QFC background. While the effect of this change on the QFC amplitude channels analyzing powers was apparently negligible (see section 4.4.2), the CKV measurement could in principle be affected since the spectrometer response function was somewhat sensitive to the beam size, and the Compton edge could move as a result of changes in the beam optics. The analyzing power tracking procedure based on monitoring the ratio of the signals in the CKV channels 6 and 7, which is routinely used in the CKV analysis, should automatically compensate for any such changes [38]. Comparison of the results obtained in the two different beam modes can be used to verify this. Figure 4.16 shows the results of the polarization measurements by three CKV and two QFC channels for the data sample used for the CKV versus QFC comparison, calculated separately for the data taken in the "narrow beam" and the "nominal beam" modes. Since the data were taken on different dates, the difference in the absolute values of the measured polarization is expected. One important conclusion is that the observed discrepancy between the CKV channels 5, 6, and 7, is unrelated to the beam optics effects.

4.5 Transverse polarization measurement

Detailed description of the transverse polarization measurement with the QFC detector is outside the scope of this thesis since it is irrelevant to the A^0_{LR} measurement. We expect to complete the analysis and publish a technical note describing the transverse polarization measurement in the future. In this section, we will only briefly discuss our experience and conclusions in this regard.

While we saw sufficient evidence that the detector is indeed sensitive to the transverse polarization, precise measurement based on the data taken during the SLD operation is hardly possible, due to a combination of the following problems :

- high background;
- lack of independent beam size information;

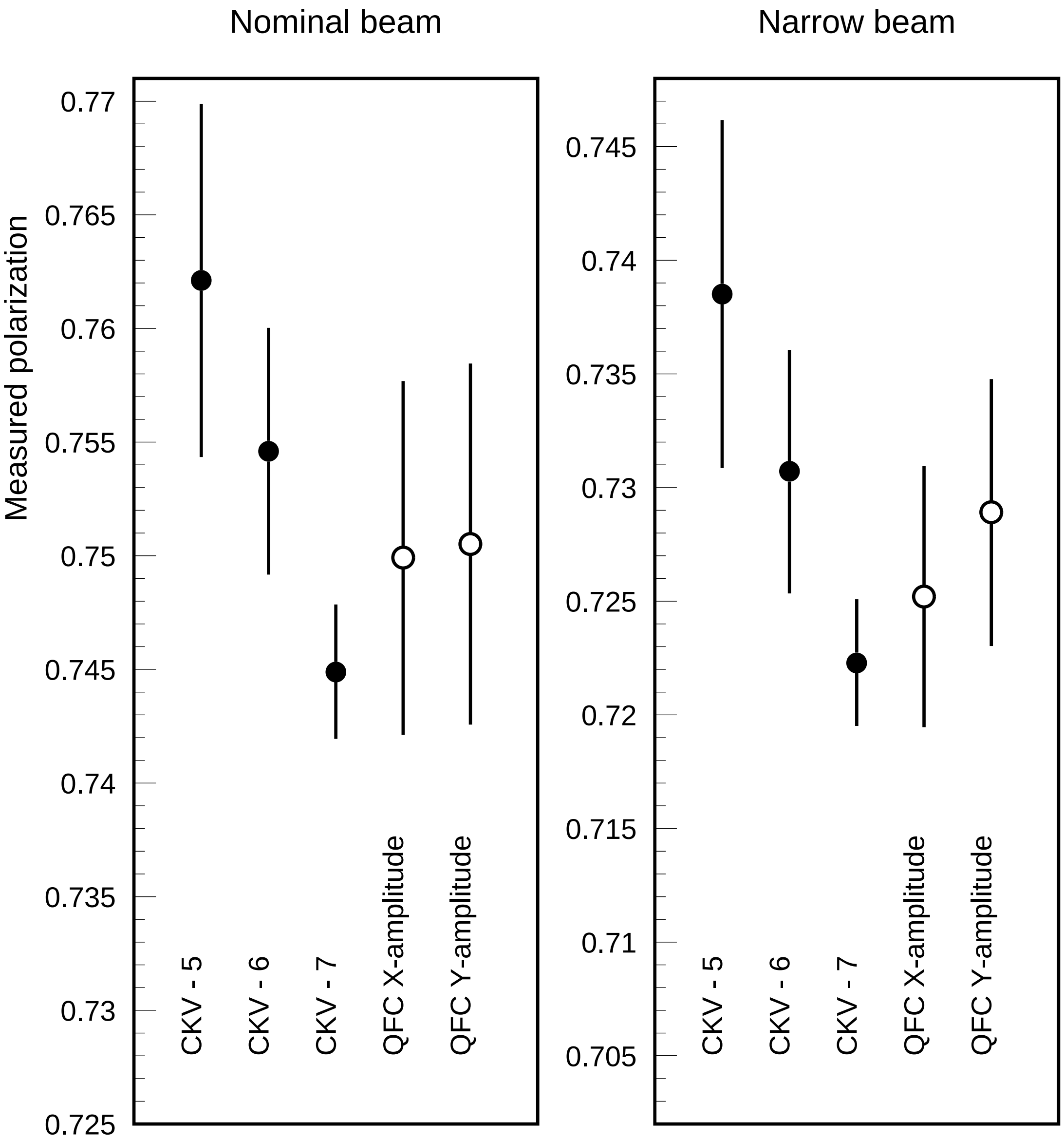

Figure 4.16: Polarization measurements with nominal and “narrow” beams. For the CKV channels, the errors shown on the plot do not include additional contributions due to the observed inter-channel inconsistency. Calibration errors for these channels have been estimated assuming 0.5 mm uncertainty in the position of the Compton edge.

- beam position instability;
- lack of precise channel to channel calibration;
- limited space available for the detector, short distance to the Compton IP;
- problems with the beam quality during the QFC beam test.

The background radiation field in the detector area was not known until we studied it with the QFC. Our original scheme for background suppression did not work because of very limited space available for the detector and unexpectedly high background from the low energy halo around the beam (see section 4.3.3 for details). Even with modified shielding configuration, signal-to-background ratio remained very low in the coordinate channels away from the shower axis. More importantly, the necessity to make room for this modified shielding forced us to remove the remotely operated micrometer stage on which the calorimeter was originally mounted (the shielding could not be located further upstream from the detector because of concerns of creating additional backgrounds for other detectors located in the area). The stage would have allowed for both horizontal and vertical movements of the calorimeter, and transverse beam scans could be used for precise cross calibration of the QFC coordinate channels. Without the stage, we had to rely on the LED calibration system for channel to channel calibration which was only accurate to a few per cent. Since this was insufficient for a direct measurement of the position difference between the Compton beams produced by the two electron-photon polarizations combinations (about 24 microns for a 100 % transversely polarized electron beam), we attempted to extract the transverse polarization by fitting the asymmetry distributions across the QFC channels. However, such asymmetry distributions were found to be sensitive to the detector angular misalignment and the size and shape of the incoming electron beam. Our ability to use the QFC itself to determine these parameters was negatively affected by the accuracy of the channel to channel calibration. We expected to have independent information on the electron beam parameters from the SLC instruments, but for the reasons not yet understood at the moment of this writing, a combination of the SLC measurements and simulations produced contradictory results for the beam configuration used during the polarization measurement with the QFC.

It should be noticed that all of the problems mentioned above can be either avoided or at least substantially reduced by designing the beam layout and the machine instrumentation from the ground up with the polarimeter in mind. This technology can certainly be used for transverse polarimeters at future collider experiments. However, keeping systematics under control is significantly more difficult than for the case of the longitudinal polarization. The longitudinal measurement using amplitude channels gets its power and low systematics from the fact that all geometrical effects (detector misalignment, local non-uniformity, beam size and shape uncertainties, etc.) cancel out from the measured asymmetry in the first order, and the analyzing power of the detector is simply equal, to a few tenth of a per cent, to the integrated asymmetry in the Compton cross section. This is not the case for the coordinate channels that are used for the transverse polarization measurement.

4.6 Results

The polarization values measured by three CKV and two QFC channels for our final data sample are listed in table 4.5

The two QFC channels are in excellent agreement with each other, and are consistent with both CKV channels 6 and 7. The CKV channel 5 had apparent instrumental problems in 1997/98 (first noticed during the QFC dedicated study), and was excluded from further analysis. Combining the measurements by different polarimeters allows for reduction of the final error of the measured polarization value used for physics analysis, as described in section 3.4.7.

Table 4.5: QFC: results of comparison to the CKV. Statistical errors are listed first. The systematic error estimates are based on the studies of relevant instrumental effects for each of the detectors. For the CKV polarimeter, the quoted systematic error does not include an additional uncertainty due to channel-to-channel inconsistency. Statistical errors in the two QFC channels are highly correlated.

Detector Channel	Measured polarization
CKV channel 5 :	$0.7442 \pm 0.0008 \pm 0.0076$
CKV channel 6 :	$0.7364 \pm 0.0006 \pm 0.0053$
CKV channel 7 :	$0.7277 \pm 0.0006 \pm 0.0027$
QFC X-amplitude channel :	$0.7311 \pm 0.0029 \pm 0.0047$
QFC Y-amplitude channel :	$0.7341 \pm 0.0031 \pm 0.0047$
QFC average :	$0.7324 \pm 0.0029 \pm 0.0044$

Chapter 5

Measuring the left-right asymmetry in Z^0 production

Measuring asymmetry in Z^0 production is simply a counting experiment:

$$A_m = \frac{N_L - N_R}{N_L + N_R} \tag{5.1}$$

where N_L and N_R are the numbers of Z^0 bosons created by left and right handed electron beam respectively. We include all Z^0 events with the exception of e^+e^- final states whose left-right asymmetry is expected to be diluted by the t-channel photon exchange.

This chapter describes the Z^0 event selection algorithm applied to the 1996 and 1997/98 runs data, and presents the estimate of the residual background. A description of a purely calorimetric event selection procedure used in the early SLD years can be found in [1] and [2].

5.1 Liquid Argon Calorimeter energy scale

Throughout the analysis described in this thesis, we use the minimum ionizing particle (MIP) based energy scale for the SLD Liquid Argon Calorimeter (LAC). The conversion factors between the measured signal (in ADC counts) and the deposited energy (in GeV) are determined by normalizing the signal produced by cosmic muons to the calculated energy deposition by a minimum ionizing particle. Since the LAC is not compensated (responses to incident MIPs, electrons, and hadrons of the same energy are different), MIP-scale energies used in this analysis do not correspond to the actual energies deposited by the final state particles in the calorimeter. For example, an average MIP-scale total energy for a hadronic Z^0 event is approximately 40 GeV. Using the MIP-scale for the A^0_{LR} analysis is advantageous since it increases separation between hadronic and e^+e^- final states.

5.2 Event selection

The major sources of potential background to be suppressed by the event selection criteria are wide angle e^+e^- final state events (Wide Angle Bhabhas, or WABs), beam related background, cosmic rays, and the two-photon events. WAB events (figure 5.1) include s-channel Z-exchange that could be a valid part of our Z^0 sample, but since it is difficult to distinguish it from other WABs, we choose to treat all Bhabhas as a background (the statistics lost due to the exclusion of the e^+e^- final states is recovered by combining the results of the A_{LR}^0 measurement with the A_e extracted from the polarized left-right forward-backward asymmetry ($\tilde{A}_{FB}^e$) measurement, as described in chapter 7). The most important contribution to the beam-related background are the SLC muons, which are produced by the off-orbit beam particles intercepted by various accelerator elements. These muons cross the detector parallel to the beam axis and therefore deposit relatively small amounts of energy in many of the LAC projective towers. Two-photon events (figure 5.2) are the result of a quark-antiquark or lepton-antilepton pair production by the two photons radiated by the incoming electron and positron. In these events, scattered electrons and positrons usually travel undetected down the beam pipe, and only the photon fusion products are registered by the detector.

The event selection is done in four stages: Pass 1, event reconstruction, Pass 2, and polarization matching.

5.2.1 Pass 1

The Pass 1 selection consists of a logical "OR" between two loose filters: the LAC-based "EIT Pass 1" [48] and the Central Drift Chamber (CDC) based "TAU Pass 1". The EIT Pass 1 filter can be described as follows. From all LAC projective towers, we select two subsets: the towers where the energy deposition exceeds the low threshold, and the towers with the energy deposition above the high threshold. The low threshold is defined as 8 ADC counts for the electromagnetic (EM) section and 12 ADC counts

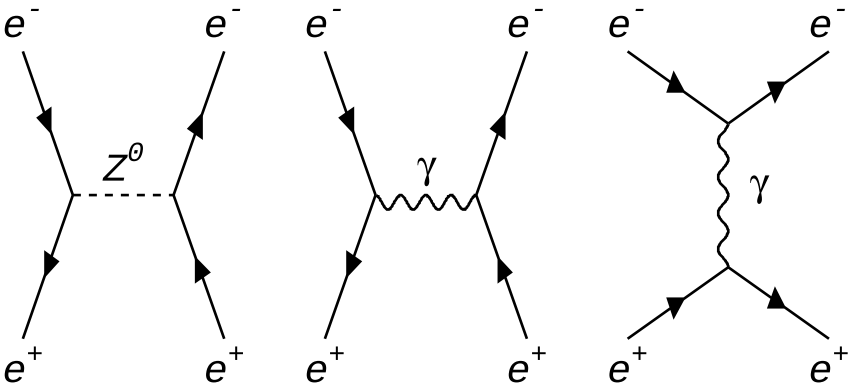

Figure 5.1: Tree level Bhabha scattering.

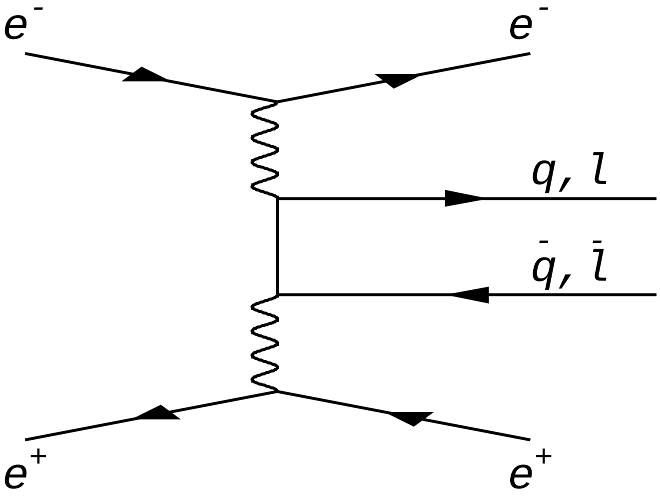

Figure 5.2: Two-photon events.

for the hadron (HAD) sections (minimum ionizing particles produce approximately 50 ADC counts and 18 ADC counts signals in the EM and HAD sections respectively per 100 MeV of deposited energy). The high threshold is 60 ADC counts for EM and 120 ADC counts for HAD sections. The sum of energy depositions in all low-threshold towers is called ELO, and a similar sum for all high-threshold towers is called EHI. To pass the EIT Pass 1 filter, the event must satisfy four requirements:

- EHI $>$ 15 GeV
- ELO $<$ 140 GeV
- EHI $> 1.5\cdot$(ELO - 70 GeV)
- there should be at least 10 EM towers in the high threshold group, with at least one such tower in each hemisphere with respect to the beam axis.

The cuts on ELO are designed to reject the beam-related background. Application of the EIT Pass 1 filter is illustrated in figure 5.3. As clearly seen on the figure, the EIT Pass 1 selection, if used alone, would have substantial inefficiency since some valid hadronic Z events could fail the ELO tests, especially during noisy SLC running conditions, and others would fall below the EHI threshold. Most of these events are picked up by the TAU Pass 1 filter, which simply requires at least one trigger-level CDC track with a momentum of at least 1 GeV/c to be found.

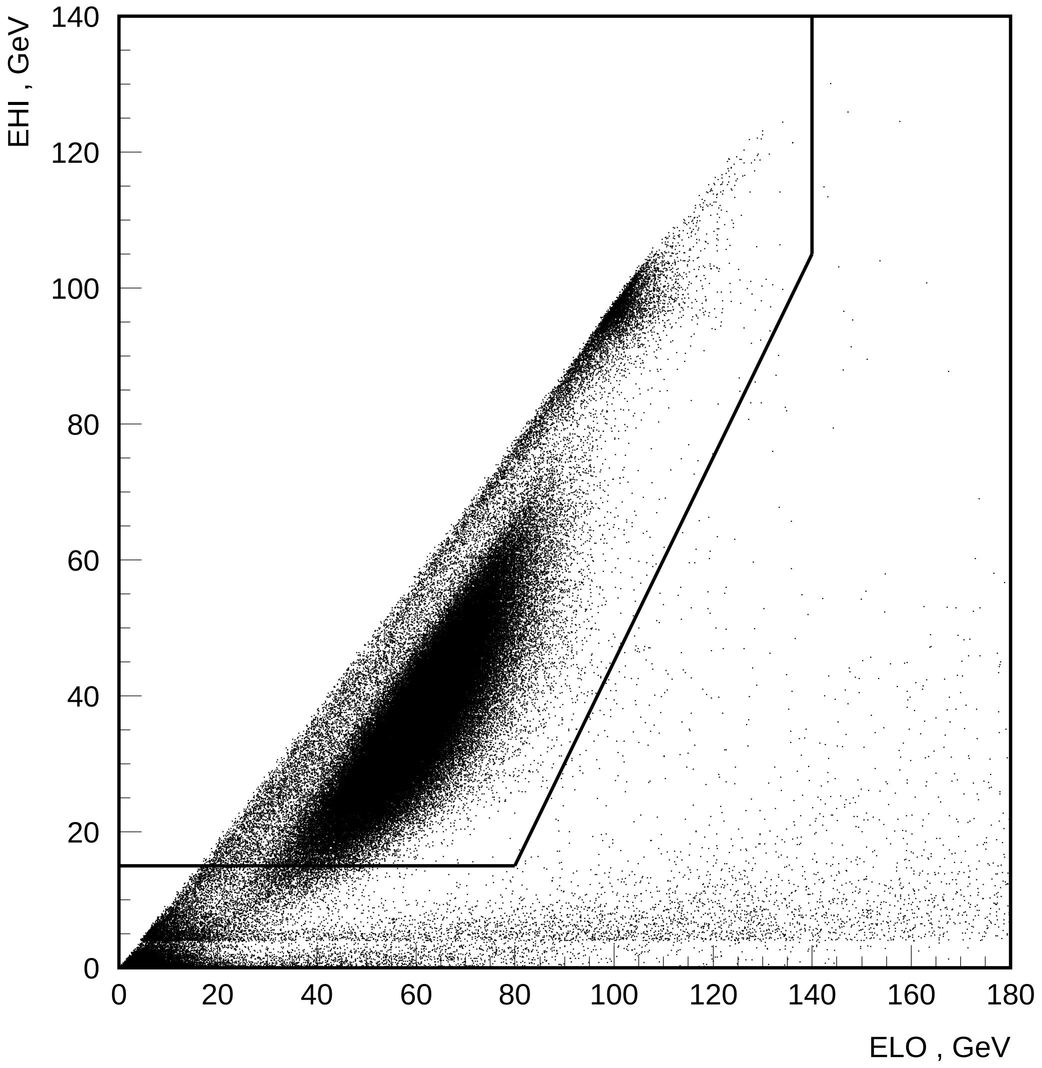

Figure 5.3: Z^0 event selection: application of EIT Pass 1 filter. EHI versus ELO for all events (1997/98 run) that satisfied TAU Pass 1 filter. EIT Pass 1 cuts are shown by lines. Bhabha events that are later removed by Pass 2 selection are centered around ELO $\approx$ EHI $\approx M_Z$.

5.2.2 Reconstruction

The events that satisfy the Pass 1 criteria are reconstructed, and clusters are identified in the calorimeter. The following quantities are defined in terms of the LAC clusters:

- total energy $E_{tot} = \Sigma E_i$;
- energy imbalance $E_{imb} = |\Sigma E_i \hat{r}_i| / E_{tot}$;

where the summation is over all LAC clusters with energies greater than 100 MeV, E_i is the energy of the i-th cluster, and $\hat{r}_i$ is a unit vector in the direction from the SLD nominal IP to the i-th cluster.

The CDC reconstruction yields two parameters used later in the event selection: n_f and n_b are the numbers of tracks in forward and backward hemispheres with respect to the direction of the electron beam. For the purpose of the A_{LR} analysis, we define a "good" CDC track as the one that has at least 100 MeV/c transverse momentum, $cos\theta \leq 0.866$ polar angle, and extrapolates to a point within 10 cm in Z and 5 cm in radius from the nominal SLD IP.

5.2.3 Pass 2 and polarization matching

The following requirements have to be met by Z event candidates in Pass 2 selection:

- $E_{tot} > 15$ GeV
- $E_{imb} < 0.6$
- $(n_f \geq 4)$ OR $(n_b \geq 4)$ OR ($(n_f \geq 2)$ AND $(n_b \geq 2)$)

Figure 5.4 shows a distribution of all event candidates from the 1997/98 run that passed the Pass 1 filter, in a E_{tot} versus E_{imb} plane. Hadronic events populate the low imbalance half of the plot, in the E_{tot} range from 20 to 60 GeV. WABs are centered at approximately 70 GeV with low imbalance. Other events (beam related background, tau pairs, etc.) tend to have higher imbalance and low total energy.

The cut on the number of tracks is designed to remove WABs (including events where a photon was radiated and later converted into a e^+e^- pair), $e^+e^- \longrightarrow \gamma\gamma$ events, and beam related background. Unfortunately, it also removes most of tau pair events. Figure 5.5 shows the same scatter plot as figure 5.4, but after applying the tracking cut.

The combined efficiency of the trigger and the event selection procedure for the 1996 and the 1997/98 runs is estimated to be (91 ± 1) % (the estimate is based on comparison with the number of small angle Bhabhas detected by the luminosity monitor). Tau pairs constitute (0.3 ± 0.1) % of the sample, the contribution from muon pairs is negligible.

In order to be useful for the A_{LR} analysis, each Z^0 event needs to be matched with the electron beam polarization value measured close in time. Polarization information may sometimes be unavailable due to high polarimeter backgrounds or hardware problems. Polarization matching reduces the Z^0 selection efficiency for the 1996 and 1997/98 runs by approximately 1 %.